MICELLAR AND LIQUID CRYSTALLINE PHASES OF SURFACTANT/PLURONIC MIXTURES STUDIED BY SANS

A Dissertation
Presented to
The Academic Faculty

by

Boyang Zhou

In Fulfillment
of the Requirements for the Degree
Master of Science
in the
The School of Materials Science and Engineering

Georgia Institute of Technology
December 2019

MICELLAR AND LIQUID CRYSTALLINE PHASES OF SURFACTANT/PLURONIC MIXTURES STUDIED BY SANS

Approve by:

Dr. Alberto Fernandez Nieves, Adviser
School of Physics
Georgia Institute of Technology

Dr. Changwoo Do, Superviser
Oak Ridge National Laboratory
Department of Energy

Dr. Valdimir Tsukruk, co-advisor
School of Materials Science and Engineering
Georgia Institute of Technology

Date Approved:
Auguest, 2019

ACKNOWLEDGEMENTS

Foremost, I would like to express my gratitude to my advisor Dr. Alberto Fernandez Nieves and the rest of my thesis committee: Dr. Changwoo Do and Dr. Vladimir Tsukruk for their continuous support for my Master study and research.

I also want to thank Dr. Changwoo Do for him always being helpful during my time working at the Oak Ridge national Laboratory.

I would like to thank my officemates Caleb and Dr. Mike T for always being helpful with my research and specifically with the writing of this thesis.

Dr. Luis Sanchez, Dr. Changwoo Do and Dr. Wei-Ren Chen, for helping me with MPB-RMSA model MATLAB fitting code.

Financial support from 'Go Student' fellowship provided by Oak Ridge National Laboratory, Department of Energy.

My family, my parents are always supportive and wise for saving up and sending me abroad, so that I could get the best education within my reach.

My girlfriend, Gaoming, for always being a wonderful person she is.

Table of Contents

LIST OF TABLES

LIST OF FIGURES

CHAPTER 1. INTRODUCTION

A Pluronic block copolymer consists of poly (ethylene oxide) (PEO) and poly (propylene oxide) (PPO) blocks that are arranged as (EO)-(PO)-(EO) with varying number of EO and PO segments. Different combinations of (EO)-(PO)-(EO) sequences result in distinct properties. One of these properties is hydrophilic-lipophilic balance (HLB). The value of HLB describes how hydrophilic an amphiphilic molecule is.[1] If HLB < 8, it is considered hydrophobic, whereas if HLB > 8, it is hydrophilic. Due to the hydrophobicity of the PPO segments, Pluronic block copolymers self-assemble into Pluronic micelles and form a micelle suspension when dissolved in water. These Pluronic micelles each have a PPO hydrophobic core and a PEO hydrophilic corona. The PPO core can provide storage space for hydrophobic drugs, while the PEO shell enhances the micelle solubility in water and provides protection against the immune system. Hence, Pluronic micelles are widely studied in drug delivery research due to their large biocompatibility.[2–4] Furthermore, Pluronic triblock copolymers are surfactants that are sensitive to impurities in solution. Pluronics are also often used in studies aimed at understanding the interaction between neutral synthetic polymers and ionic surfactants. [5–8]

Among the Pluronic family, L62 [(EO)6-(PO)34-(EO)6] has a much shorter chain length and it is more hydrophobic than L64 (PO/EO=15:13); (HLB=15) and F127 (PO/EO=7:20); (HLB=22), due to its higher PO/EO ratio (PO: EO=17:6); (HLB=6). The main merit of L62 is that it retains the micellar self-assembling ability when mixed in water as the larger Pluronics, but the micelle size is smaller than 100nm, making it an appropriate candidate

for blood capillary drug delivery or for infiltration through organ barriers.[9,10] Based on previous studies, L62 forms micelles in water at room temperature. However, at temperatures above 60C, the solvent quality of water decreases dramatically for the EO segments such that they prefer to interact with other EO segments than with water molecules. This results in a phase transition from a micellar phase to phase consisting of polymer rich and polymer poor regions.[1] In addition, L62 has a lower CMT compared to other Pluronics and a higher cloud point due to its high hydrophobicity.

Mixed micelles of an ionic surfactant and a neutral hydrophilic polymer are commonly studied to improve upon the drug encapsulation ability of either pure component. One example of this is Sodium dodecyl sulfate (SDS) with Pluronic F127.[11] In this case, mixed micelles incorporate both components at sufficiently high concentration. But both components are hydrophilic, so the stability of SDS/F127 mixed micelles is limited when dissolved in water.

In contract to SDS, the Aerosol-OT (AOT) ionic surfactant is more hydrophobic and forms liquid crystal lamellar (LLC) structures in water, which are persistent even around the boiling temperature of water.[12] In the study of polymer-surfactant interactions, the AOT LLC is usually selected as the ideal host structure for hydrophilic polymers, such as polyethylene oxide (PEO).[9,13,14] In mixtures of AOT and PEO_6 (6 EO segments), large amounts of PEO can be dissolved in the aqueous domains of the AOT lamellar phase at room temperature. With a longer PEO chain, like PEO_{30}, the AOT lamellar phase is no longer suitable for storing PEO chains and the PEO is expelled from the LLC water domains.[12] As a result, the AOT lamellar phase and a PEO isotropic solution phase coexist. However, there is no evidence showing PEO has any significant influence over the stability

of the AOT lamellar phase with temperature, on its periodicity, nor on the lamellar phase compressional modulus.

While references to mixtures between ionic surfactant and hydrophilic polymer exist, including AOT/PEO and SDS/F127, similar studies about hydrophobic polymer and ionic surfactants are rare. However, based on previous studies of AOT/PEO mixture, it may seem reasonable to expect that L62 and AOT will not mix when dissolved in water. The AOT can be expected to maintain its LLC structure, since the EO segments in L62 chains are unlikely capable destabilizing the structure. In fact, according to studies on PEO/AOT systems, L62 is less likely to be contained in the AOT aqueous region, especially at high temperatures. Furthermore, due to the high PO/EO ratio, the hydrophobicity prevents L62 micelles from breaking down into unimers to interact with the ionic surfactant, as occurs in F127/SDS mixtures.[7] Therefore, the AOT/L62 system can be expected to consist of an AOT lamellar phase and a L62 micellar phase separated from each other. However, despite L62 and AOT both being hydrophobic, there are hydrophilic segments on both L62 and AOT. Hence, it is still possible that the AOT and L62 will form mixed micelle structures, which are expected to be more stable in water.

In our experiment, we mix 5wt% in total of L62 and AOT in water within a temperature ranging from 10℃ to 70℃ at different relative concentrations. Surprisingly, we see that the two hydrophobic polymers form L62/AOT mixed micelles in water. Indicated by experimental data, the AOT lamellar structure breaks into monomers and, at the same time, participates in the L62 polymer self-assembly process to form mixed micelles. The number of AOT monomers in micelles is monitored by the effective charge number in the mixed micelles. At a relative concentration L62/AOT of 25wt%, from 10℃ to 20℃, only the AOT

lamellar structure is present but as the temperature increases from 20℃ to 70℃, the degree of micellization increases along with the charge number, indicating the growth of the L62-rich mixed micellar phase. As will be shown later, the micelle phase appears with increasing temperature together with the disappearance of the AOT lamellar phase. We suspect that at higher temperatures, the hydrophilic head groups of AOT prefer to mix with the EO segments because of the poor solvent quality, resulting in hydrophilic polymer chains tending to interact with each other instead of with the solvent molecules. Similarly, the AOT tail groups would mix more with the PO segments, due to hydrophobicity. Such combination is energetically favored for both, especially at high temperature, where the AOT lamellar and L62 micelle phase are less stable. At L62/AOT 50wt% and 75wt%, the AOT LLC disappears above 15℃, while the mixed micellar structure persists from ~15℃ up to 70 ℃, which is significantly higher than the corresponding phase transition temperature of pure L62. We also notice that the temperature at which mixed micelles start to form is much lower than the CMT of pure L62 micelles, and the size of the mixed micelles is smaller than pure L62 micelles and does not vary significantly compared to the pure micelles at high temperatures. Based on our understanding of the AOT/L62 system, the mixing behaviors of this hydrophobic ionic surfactant and hydrophobic polymer is generally different from hydrophilic SDS mixing with hydrophilic polymers. Our results enable us to understand the consequences of the interactions in the system. We present in the following sections, the detailed analysis and discussion.

CHAPTER 2. INTRODUCTION TO SLS

SLS stands for static light scattering experiment. In SLS, the time independent scattering intensity is studied. The time averaged coherent scattering intensity of an N-component system of spherically symmetric particles is written as[15],

$$\frac{d\Sigma}{d\Omega} = V^{-1}\left\langle \sum_{j=1}^{N} \sum_{i=1}^{N} \langle F_j(q) F_i^*(q) \rangle \exp\left[-iq\left(R_j - R_i\right)\right] \right\rangle \quad (1)$$

Where $F_j(q)$ is the scattering amplitude of j^{th} particle and R_j is the distance between the j^{th} particle and origin. $\exp\left[-iq\left(R_j - R_i\right)\right]$ accounts for interparticle scattering, which contains structure information among particles. Detailed derivation of Eq.1 will be presented in the next chapter and it will be shown that Eq.1 can be reduced to,

$$\frac{d\Sigma}{d\Omega} = n_p P(q) S'(q) \quad (2)$$

n_p is the number density of particles, $P(q)$ is the form factor of a single scatter and $S'(q)$ is the apparent structure factor[16].

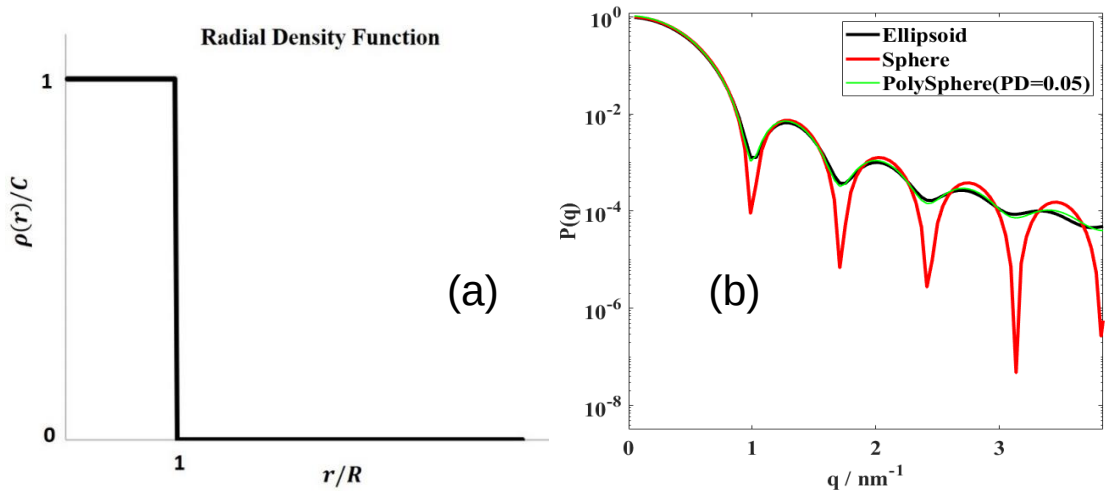

Fig.2.1. (a) Density profile for a homogeneous sphere solution shown in Eq.1. (b) Red line shows the form factor $P(q)$ from Eq.6 plotted against q (nm^{-1}). Green line represents the polydisperse sphere form factor with polydispersity of 5%, Eq.7. Black line represents the Ellipsoid of revolution form factor based on Eq.10

In the following sections, three form factor models are discussed; Homogenous Sphere model, Ellipsoid of revolution and Debye function for Gaussian chains. Fig.2.1 compares some of these models.

2.1 Form Factor Model: Homogeneous Sphere

The homogeneous sphere model is the simplest of these three models. Particles in the homogeneous system have the same size and the radial density function is defined to be[17]:

$$\rho(r) = \begin{cases} C, & r \leq R \\ 0, & r > R \end{cases} \tag{3}$$

$\rho(r)$ is plotted in Fig.1(a). r is the distance from the particle center and constant C has unit of density. R is the radius of the homogeneous sphere. The amplitude of the field scattered by a single particle is written as,

$$A(q) = 4\pi \int_0^\infty \rho(r) \frac{\sin(qr)}{qr} r^2 dr = 4\pi \int_0^R \frac{\sin(qr)}{qr} r^2 dr\,,\ r \leq R$$

$$= \frac{4\pi}{q} \int_0^R \sin(qr) r dr \tag{4}$$

After performing partial integration, we get,

$$= \frac{4\pi}{q} \left(-\frac{Rcos(qR)}{q} + \left[\frac{\sin(qr)}{q}\right]_0^R \right)$$

$$= \frac{4\pi}{q} \left(\frac{\sin(qR)}{q^2} - \frac{Rcos(qR)}{q} \right)$$

$$= \frac{4\pi}{q^3} (\sin(qR) - qRcos(qR))$$

$$= \frac{4}{3}\pi R^3 \frac{3[\sin(qR) - qRcos(qR)]}{(qR)^3} \tag{5}$$

and after normalization at $A(q = 0)$,

$$F(q = 0) = \frac{A(q=0)}{V} = 1 \tag{6}$$

$$F(q) = \frac{3[\sin(qR) - qR\cos(qR)]}{(qR)^3} \quad (7)$$

$F(q)$ is the form factor amplitude of single particle and the form factor intensity equals to $P(q)_{HS} = F^2(q)$, omitting the prefactors,

$$P(q)_{HS} = \left(\frac{3[\sin(qR) - qR\cos(qR)]}{(qR)^3}\right)^2 \quad (8)$$

In a polydisperse system, the spheres have a distribution of radius. The polydisperse form factor can be written as an integral over the monodisperse form factor multiplied by some distribution, such as a Gaussian;

$$P(q) = \frac{1}{\sqrt{2\pi\sigma}} \int P_i(q, R_i) \exp\left[-\frac{1}{2}\left(\frac{R_i - \langle R\rangle}{\sigma_P}\right)^2\right] dR_i \quad (9)$$

Where $P_i(q, R_i)$ is the form factor of monodisperse form factor from Eq.6 and R_i has a range of value, $(|\langle R\rangle - 3\sigma_P| < R_i < \langle R\rangle + 3\sigma_P)$. $\langle R\rangle$ is the mean particle radius and $\sigma_p = PD * \langle R\rangle$ is the standard deviation of the particle radius respect to the mean radius and PD stands for the polydispersity. From Eq.8 and Eq.9, we can see that $P(q)$ has zero values when $tanqR = qR$, where $qR = 4.49, 7.73, \ldots$ so we can plot the Form factor intensity versus q, then divide 4.49, 7.73… by the q value where intensity $P(q)$ has minimums to estimate the radius of the spheres.[18] The form factor of homogeneous sphere $P(q)$ from Eq.8 is plotted using hard core radius $R = 4.49\,nm$. The position of the minimums are $qR = 4.49, 7.73, \ldots$ and with $R = 4.49\,nm$, leaving the minimums of $P(q)$ at $q = 1, 1.72, \ldots (nm^{-1})$, as shown in Fig.1. The maximums of the form factor result from the constructive interference of the scattered radiations by the spheres. With 5% polydispersity of the radius, the minimums of the monodisperse sphere are washed out and the positions of the maximums are suppressed compared to those of the monodisperse model.

2.2 Form Factor Model: Ellipsoid of Revolution

An extension of homogeneous sphere model is the Ellipsoid of revolution model. In this model, the polar radius R_p is along the rotational axis Z and equatorial radius R_e extends along X and Y axis, as shown in Fig.2 The scattering amplitude of a fixed orientation particle with respect to $\vec{q}$ is written as,[19]

$$F_{ellip}(q,\alpha) = \frac{3[sinqr - qrcos(qr)]}{(qr)^3} \tag{10}$$

$$r = \sqrt{R_e \sin^2\alpha + R_p^2 \cos^2\alpha} \tag{11}$$

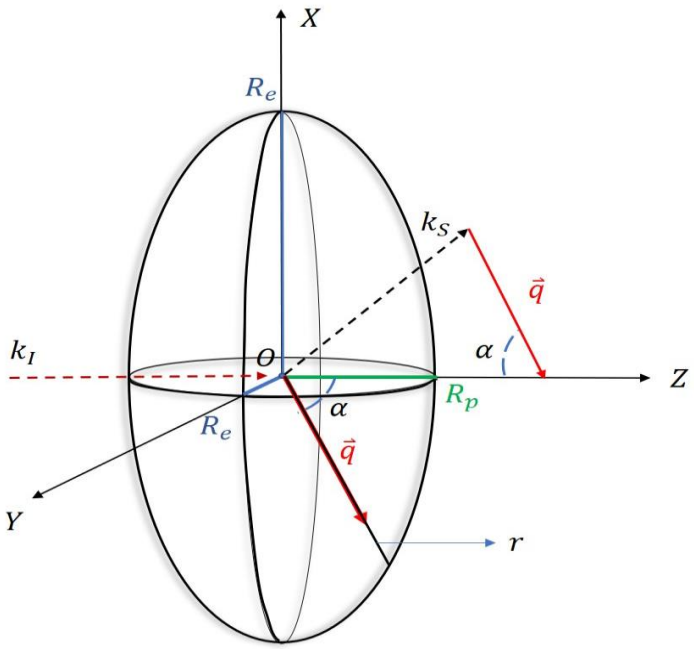

Fig.2.2. The schematics of the ellipsoid of revolution being impinged by the incident wave k_I is plotted. This ellipsoid of revolution represents the general form of a micelle that is investigated in our experiment. Ellipsoid aligns and rotates along Z axis and sweeps in the $X - Y$ plane.

In Fig.2.2, The incident radiation k_I propagates along the Z axis and is then scattered at the origin O. k_S is the scattered radiation and the scattering vector $\vec{q}$ is defined $\vec{q} \equiv k_S - k_i$. r is the line segment originated from the center of the ellipsoid to a point at the surface of

the ellipsoid along the vector $\vec{q}$. α is the angle between the scattering vector $\vec{q}$ and the rotational axis of the ellipsoid. Following the Pedersen's review[20], we can perform orientational average to the scattering intensity of random oriented particles,

$$F_{ellip}^2(q) = \int_0^{\pi/2} F_{ellip}^2(q,\alpha)\sin(\alpha)d\alpha \tag{12}$$

$$P_{ellip}(q) = F_{ellip}^2(q) \tag{13}$$

The form factor of the ellipsoid of revolution is plotted with the form factor of the homogeneous sphere. The result is shown in Fig.1 and we can tell that the ellipsoid model scatters in a very similar manner to the model of polydisperse spheres; the minimums of the Ellipsoid form factor are being washed out due to destructive interference. Additionally, the maximums of $P(q)$ are suppressed, and the positions of them are vary, compared to monodisperse hard spheres.

2.3 Form Factor Model: Polymer Excluded Volume Model

In the small angle neutron scattering experiment, the scattering intensity at high Q range sometimes is dominated by molecular structure of particles, which is the polymer chain network in our case. Consider polymer chains in the solvent, where each monomer pair is separated by the distances r_{ij} and r_{ij} which follow the Gaussian chain statistics[21],

$$P(r_{ij}) = \left(\frac{3}{2\pi\langle r_{ij}^2\rangle}\right)^{3/2} \cdot \exp\left(-\frac{3r_{ij}^2}{2\langle r_{ij}^2\rangle}\right) \tag{14}$$

$\langle r_{ij}^2\rangle$ is the variance described by the segment length a,

$$\langle r_{ij}^2\rangle = a^2|i-j|^{2\upsilon} \tag{15}$$

υ is the excluded volume parameter, which is related to the Porod exponent μ as $\mu = \frac{1}{\upsilon}$. The single chain form factor is written as,

$$P(q) = \frac{1}{n^2}\sum_{i,j}^{n}\langle\exp(-i\vec{q}\cdot r_{ij}^2)\rangle \tag{16}$$

$$= \frac{1}{n^2}\sum_{i,j}^{n}\int d\overrightarrow{r_{ij}}P(r_{ij})\,exp\left(-i\vec{q}\cdot\overrightarrow{r_{ij}}\right) \quad (17)$$

$$P(q) = \frac{1}{n^2}\sum_{i,j}^{n} exp\left(-\frac{q^2\langle r_{ij}^2\rangle}{6}\right) = \frac{1}{n^2}\sum_{i,j}^{n} exp\left(-\frac{q^2a^2|i-j|^{2\upsilon}}{6}\right) \quad (18)$$

where n is the number of chain segments and when $n \gg 1$, we can write Eq.18,

$$P(q) = \frac{1}{n^2}2\sum_{k=1}^{n}(n-k)exp\left(-\frac{q^2a^2}{6}k^{2\upsilon}\right) \quad (19)$$

If we then take the continuous limit of Eq.19 we can write,

$$P(q) = 2\int_0^1(1-x)\exp\left(-\frac{q^2a^2}{6}n^{2\upsilon}x^{2\upsilon}\right)dx \quad (20)$$

Where $x = k/n$. Eq.20 can be expressed in terms of the gamma function:

$$\Gamma(x) = \int_0^{U=\infty}\exp(-t)\,t^{x-1}\,dt \quad (21)$$

$$U = \frac{q^2R_g^2(2\upsilon+1)(2\upsilon+2)}{6} \quad (22)$$

Then the form factor of a polymer chain is written as,

$$P(q) = \frac{1}{\upsilon U^{\frac{1}{2\upsilon}}}\Gamma\left(\frac{1}{2\upsilon}\right) - \frac{1}{\upsilon U^{1/2\upsilon}}\Gamma\left(\frac{1}{\upsilon}\right) \quad (23)$$

And radius of gyration R_g, which measures the distribution of mass inside particles, is defined as,

$$R_g = \sqrt{\frac{a^2n^{2\upsilon}}{(2\upsilon+1)(2\upsilon+2)}} \quad (24)$$

When a polymer chain dissolves in the theta solvent, it behaves like an ideal chain that follows the Gaussian chain statistics and has a fractal dimension of 2. In this case, $\upsilon = 0.5$ and Eq.23 can be reduced to,

$$P(q) = \frac{2}{q^4R_g^4}\left(\exp\left(-q^2R_g^2\right) - 1 + q^2R_g^2\right) \quad (25)$$

Eq.25 is known as the Debye function of the Gaussian chains and the inverse of $P(q)$ can be plotted against $(R_g * Q)^2$ for the purpose of approximating its value at low q and high

q range, the result is shown in Fig.2.3(a). The inverse value of the Debye function Eq.25 is plotted against $(R_g * Q)^2$ and the y-intercept is adjusted to 1. At low q range, a straight line with a slope of $1/3$ can catch the trend of inverse Debye function accurately and at higher q range, a straight line with a slope of $1/2$ can accurately describe the inverse Debye

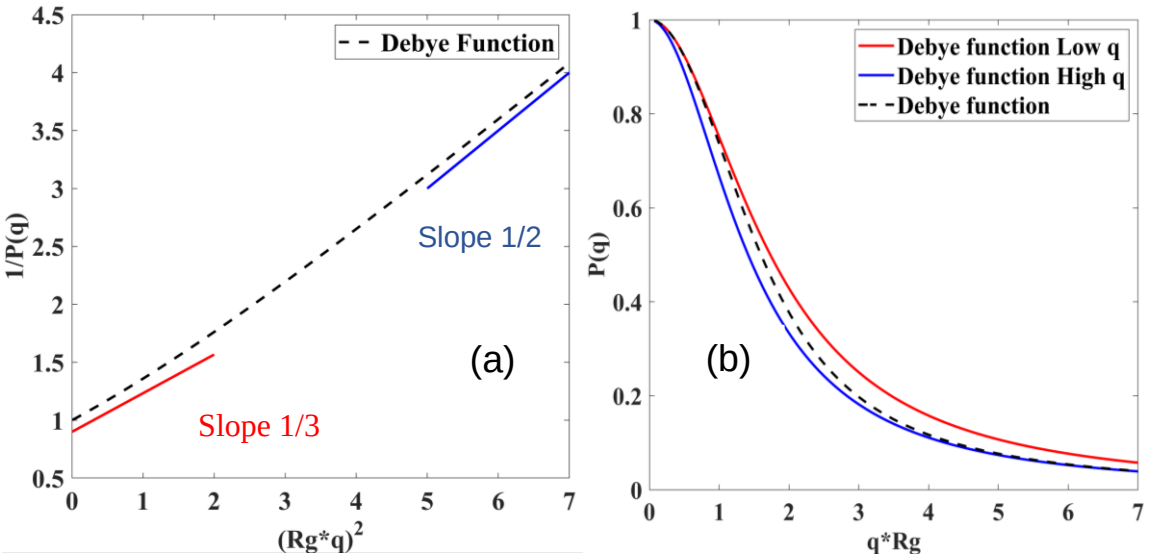

Fig.2.3, (a) The inverse value of the form factor of Gaussian chain $1/P(q)$ is a linear function respect to $(R_g * q)^2$ at both $qR_g \ll 1$ and $qR_g \gg 1$ with different slopes. (b) The Debye function Eq.22 (black dash line) is plotted against its approximation at low Q range Eq.24 (red line) and at high Q range Eq.25 (blue line).

function. We can then approximate Debye function with the Lorentzian form of q-dependence of scattering intensity[22],

$$P(q) \propto \frac{1}{1+(q\xi)^2} \tag{26}$$

Where ξ is the local blob size of the polymer chain, where the polymer chain is divided into consecutive blobs with diameter ξ and at length scale below ξ, the polymer chain behaves as an idea chain. In Fig.2.3, the slope of the inverse Debye function at low q is $1/3$ and we can thus approximate $\xi \approx R_g/\sqrt{3}$. Similarly, we can approximate $\xi \approx R_g/\sqrt{2}$ at high q range. Hence, we can write,

$$P(q) \propto \frac{1}{(1+\frac{q^2R_g^2}{3})}, \qquad qR_g \ll 1 \tag{27}$$

$$P(q) \propto \frac{1}{(1+\frac{q^2R_g^2}{2})}, \qquad qR_g \gg 1 \tag{28}$$

Eq.27 and Eq.28 approximate the Debye function at low and high q and the results are summarized in Fig.2.3(b). The region in which the approximation Eq.27 is valid is called the Guinier regime, and the valid region for Eq.28 is called the Porod regime. Adding the ellipsoid form factor and the Debye function together, and including the constant term I_{bg} to account for the background scattering, gives the final form factor we use to describe the micelles,

$$P(q) = C_1 \int_0^{\frac{\pi}{2}} F_{ellip}^2(q,\alpha)\sin(\alpha)\,d\alpha + C_2 \frac{2}{q^4R_g^4}\left(\exp\left(-q^2R_g^2\right) - 1 + q^2R_g^2\right) + I_{bg} \tag{29}$$

$P(q=0) = 1$, by definition. Since the form factor of the ellipsoid dominates the low q range, we can meet the definition by setting $C_1 = 1$. The second term, which is the Debye function, mainly accounts for the form factor at high q. In our experiment, we let $C_2 = C(1 - f_{mic})$, where C is the total polymer concentration (number of polymer chain per unit volume) and f_{mic} is the polymer fraction forming micelles, so $1 - f_{mic}$ is the fraction of unimers in the solvent.

CHAPTER 3. INTRODUCTION TO STRUCTURE FACTOR

3.1 The (Grand) Canonical Ensemble

In thermodynamics, the canonical ensemble is a useful tool for calculating thermodynamic properties (entropy, free energy) of a system. Consider a glass of water consisting of N molecules of water taking up a volume, V. The water's macroscopic properties can be specified with few parameters, such as volume, density and temperature, but the microscopic properties cannot. From a microscopic perspective, an N-body system could be in any of the 10^N (more like ~V^N?) possible quantum states that exhibit would demonstrate the measured macroscopic properties, which makes the calculation of microscopic properties impossible. The concept of an 'ensemble of system' is therefore introduced. An ensemble, A, contains replicas (or microstates?) of the N-body system with volume V that correspond to each of the possible quantum states. The canonical ensemble is an ensemble that is mechanically isolated, but free to exchange heat with a large reservoir that is held at a constant temperature. By calculating an average of a thermodynamic variable (such as pressure or energy) across all possible replicas, the thermodynamic properties of the system can be predicted. [23]

The grand canonical ensemble is more general than the canonical ensemble. In this case, particles can also be transported through the system boundaries, in addition to heat. Hence, for each value of N, there is a set of energy states $\{E_{Nj}(V)\}$. The occupation number a_{Nj} denotes the number of systems with N particles that are in the microstate j. a_{Nj} is not unique and the set $\{a_{Nj}\}$ is thus a distribution of a_{Nj}. We assume that all possible states in

the distribution should be weighed equally and the distributions should satisfy the following conditions,[24]

$$\sum_N \sum_j a_{Nj} = \mathrm{A} \tag{1}$$

$$\sum_N \sum_j a_{Nj} E_{Nj} = E_{fixed} \tag{2}$$

$$\sum_N \sum_j a_{Nj} N = N_{tot} \tag{3}$$

A, E_{fixed} and N_{tot} are the number of microstates in the ensemble, the total energy of the ensemble, and total number of particles in the ensemble, respectively. The number of ways $W(\{a_{Nj}\})$ to arrange A distinguishable systems into a set $\{a_{Nj}\}$ is,

$$W(\{a_{Nj}\}) = \frac{\mathrm{A}!}{\prod_N \prod_j a_{Nj}!} \tag{4}$$

Based on Eq.1-3, we can then write the probability of choosing any system that contains N particles in state j with energy E_{Nj} as $P_{Nj}(V,T,\mu)$,

$$P_{Nj}(V,T,\mu) = \frac{a^*_{Nj}}{\mathrm{A}} = \frac{e^{-\beta E_{Nj}(V)} e^{-\mu N/kT}}{\sum_N \sum_j e^{-\beta E_{Nj}(V)} e^{-\mu N/kT}} \tag{5}$$

$\{a^*_{Nj}\}$ is the most probable distribution, which maximizes the $W(\{a_{Nj}\})$ and Eq.5 can be rewritten as,

$$P_{Nj}(V,T,\mu) = \frac{e^{-\beta E_{Nj}(V)} e^{-\mu N/kT}}{\Xi(\mathrm{V,T,\mu})} \tag{6}$$

Where $\Xi(V,T,\mu)$ is the grand partition function and can be described via partition function $Q(N,V,T)$,

$$\Xi(V,T,\mu) = \sum_N \sum_j e^{-\beta E_{Nj}(V)} e^{-\mu N/kT} = \sum_N Q(N,V,T) e^{-\mu N/kT} \tag{7}$$

3.1.1 Ideal Monotonic Gas and Imperfect Gases

The canonical partition function $Q(N,V,T)$ can be written as a summation in a system with a small number of particles and discrete energy levels, Eq.7. However, as more particles are included in the system, it is easier to consider $Q(N,V,T)$ in an integral form, [25]

$$Q = \frac{1}{N!h^{3N}} \int \cdots \int e^{-\beta H} dp_1 \cdots dp_N dr_1 \cdots dr_N \tag{8}$$

where H is the Hamiltonian,

$$H = \frac{1}{2m} \sum_{n=1}^{N} \left(p_{xn}^2 + p_{yn}^2 + p_{zm}^2\right) + U(x_1, y_1, \cdots, z_N) \tag{9}$$

Plugging Eq.9 into Eq.8, we can solve for the partition function,

$$Q(N,V,T) = \frac{1}{N!} \left(\frac{2\pi mkT}{h^2}\right)^{3N/2} Z_N \tag{10}$$

Where Z_N is the configurational integral that describes all possible configuration of N particles being in the position $dr_1 \cdots dr_N$,

$$Z_N = \int \cdots \int e^{-U_N/kT} dr_1 dr_2 \cdots dr_N \tag{11}$$

For ideal gas, or for real gasses with a low enough density, particles don't interact. As a result, we can ignore the potential term U_N in Z_N, so $Z_N = V^N$ and $Q = q^N/N!$, where $q(V,T) = (2\pi mkT/h^2)^{3/2}V$. However, for non-ideal gasses at higher densities, we can no longer neglect the interparticle potential.

3.1.2 Distribution Function of Liquid in Closed Systems

For a non-ideal gas, we can perform pressure expansion in term of the density of the system, so that the many-body problem can be reduced into a two-body, three-body problem, which is simpler to solve for thermodynamic properties. However, for a liquid, such decomposition is not applicable, since liquid molecules are constantly interacting with

large numbers of their neighbors. Under this circumstance, the radial distribution function becomes key. Consider a closed system containing N particles in a volume V at Temperature T. The probability that particle 1 is in dr_1 at r_1, particle 2 is in dr_2 at r_2 … [26]

$$P^{(N)}(r_1, \ldots, r_N)dr_1 \ldots dr_N = \frac{e^{-\beta U_N}\, dr_1 \ldots dr_N}{Z_N} \tag{12}$$

Where Z_N is the configuration integral, which is the sum of all possible configurations of N-particle system. U_N is the interaction potential among all N of the liquid molecules. In our study of study of our micelle system, the potential is considered as hard sphere Yukawa potential.

In a liquid, unlike in a crystal, the positions of the molecules are indistinguishable. The probability of particle 1 being located at r_1 ⋯ particle n being located at r_n, irrespective of the configuration of the remaining N-n particles can be denoted by integrating over n+1 particle through N,

$$P^{(n)}(r_1, \ldots, r_n) = \frac{\int \ldots \int e^{-\beta U_N}\, dr_{n+1} \ldots dr_N}{Z_N} \tag{13}$$

If the probability that any of the N particles are within dr_n of r_n is independent of the locations of the rest of the particles, then

$$\rho^{(n)}(r_1, \ldots, r_n) = \frac{N!}{(N-n)!} \cdot P^{(n)}(r_1, \ldots, r_n) \tag{14}$$

In liquid, the probability that finding one particle in dr_1 is $\rho^{(1)}(r_1)dr_1$. Considering that every position in the liquid system with volume V is equivalent, we know the probability $\rho^{(1)}(r_1)dr_1$ is independent of r_1. Therefore, for a liquid, we can write equation,

$$\frac{1}{V}\int \rho^{(1)}(r_1)dr_1 = \rho^{(1)} = \frac{N}{V} = \rho^1 \tag{15}$$

Based on Eq.15, we are safe to assume that in the volume V, the probability that finding each one of the n independent particles in dr_n is,

$$\rho^{(n)}(r_1, \dots, r_n) = \rho^n \tag{16}$$

Based on Eq.16, we can now define the n particle correlation function $g^{(n)}(r_1, \cdots, r_n)$ as,

$$\rho^{(n)}(r_1, \dots, r_n) = \rho^n g^{(n)}(r_1, \cdots, r_n)$$

$$g^{(n)} = \frac{\rho^{(n)}}{\rho^n} \tag{17}$$

If every position of every particle in the volume V is truly independent, $\rho^{(n)}(r_1, \dots, r_n)$ simply equals to ρ^n, shown in Eq.16. Therefore, $g^{(n)}$ is the correlation function of n particles, that accounts for the correlation among those particles.

3.1.3 Distribution Function of Liquid in Open Systems

To generalize the distribution function $\rho^{(n)}(r_1, \dots, r_n)$, we must consider it in open systems. In open systems, there is not a constant number of particles. Therefore, we must take the possibility that system contains N particles into our consideration. The possibility of finding n particles that independent with N particles in $dr_1 \cdots dr_N$, at $r_1 \cdots r_N$ in open system is,[26]

$$\rho^{(n)} = \sum_{N \geq n} \rho_N^{(n)} P_N \tag{18}$$

$\rho_N^{(n)}$ is the $\rho^{(n)}$ we derived in closed N particle system, as shown in Eq.16. P_N is the possibility of a system containing N particles,

$$P_N = \frac{Q(N,V,T)e^{-\mu N/kT}}{\Xi(V,T,\mu)} = \frac{z^N Z_N}{N!\Xi} \tag{19}$$

The numerator of Eq.19 is the partition function from the canonical ensemble that contains all the systems that has N particles in volume V in thermal equilibrium at temperature T, while the denominator $\Xi(V, T, \mu)$ is the partition function derived in grand canonical ensemble, which can be seen as a collection of canonical ensembles in thermal equilibrium

but contains all possible value of N. Therefore, Eq.19 gives us the probability that an open system contains N particles. Further, plugging Eq.10 into Eq.19, it can be simplified into its final form, where $z = \left(\frac{2\pi mkT}{h^2}\right)^{3/2}$. Substituting Eq.13 and 14 into Eq.18 gives,

$$\rho^{(n)}(r_1, \dots, r_n) = \frac{1}{\Xi}\Big\{z^n e^{-\beta U_n} + \sum_{N=n+1}^{\infty} \frac{z^N}{(N-n)!} \int \dots \int e^{-\beta U_N}\, dr_{n+1} \dots dr_N\Big\} \quad (20)$$

We can then apply Eq.17 to derive the radial distribution function $g^{(n)}(r1, \cdots r_N)$,

$$g^{(n)}(r_1, \cdots r_N) = \frac{V^n}{\Xi \mathrm{N}^n}\Big\{z^n e^{-\beta U_n} + \sum_{N=n+1}^{\infty} \frac{z^N}{(N-n)!} \int \dots \int e^{-\beta U_N}\, dr_{n+1} \dots dr_N\Big\} \quad (21)$$

In our experiment, the radial distribution function of two particle $g^{(2)}(r_1, r_2)$ is particularly important since it can be determined experimentally via scattering experiment. Since $g^{(2)}(r_1, r_2)$ depends solely on the relative distance between particle 1 and 2, r_{12}, we can drop the scripts and write $g^{(2)}(r_1, r_2)$ as $g(r)$. $g(r)$ describes the probability that finding a particle at distance r in dr from another particle and it is known as pair correlation function.

3.1.4 Determining Radial Distribution Function $g(r)$ via Scattering Experiment

$$P(\theta) = \frac{I(\theta)}{I(0)} \propto \sum_i \sum_j \frac{\sin(qr_{ij})}{qr_{ij}} \quad (22)$$

Where $I(\theta)$ is the scattering intensity through angle θ and $I(0)$ is the transmitted intensity. $P(\theta)$ can be measured experimentally and it contains the information about the

configuration of collection of scatters. $q = (4\pi/\lambda)\sin(\theta/2)$ is the scattering vector. For a liquid, the r_{ij} are continuously distributed and Eq.22 can be written in integral form,[27]

$$P(\theta) \propto \int_0^\infty 4\pi r^2 g(r) \frac{\sin(qr)}{qr} dr \tag{23}$$

Eq.23 can be further rewritten as,

$$P(\theta) \propto \int_0^\infty 4\pi r^2 (g(r) - 1) \frac{\sin(qr)}{qr} dr + \int_0^\infty 4\pi r^2 \frac{\sin(qr)}{qr} dr \tag{24}$$

When we integrate Eq.24, the second integral vanishes at $q \neq 0$,

$$P(\theta) \propto \int_0^\infty 4\pi r^2 (g(r) - 1) \frac{\sin(qr)}{qr} dr \propto \int (g(r) - 1) e^{iqr} dr \tag{25}$$

We let $g(r) - 1 = h(r)$. The product of the Fourier transform of $h(r)$ and the density, ρ, is called the structure factor of the liquid. It is dependent with q, the scattering vector,

$$S(q) = \rho \int h(r) e^{iqr} dr \tag{26}$$

The significance of the pair correlation function $g(r)$ is that we can interpret the configurations and the interactions among the molecules in the real space. By performing the scattering experiment, we can determine the structure factor $S(q)$ from the scattering intensity, which describes the structure of a collection of scatters in momentum space and we can then relate $S(q)$ to $g(r)$ via Fourier transform, as shown in above.

3.1.5 Direct Correlation Function of Liquid

$h(r_{12})$ measures the total influence that particle 1 has on particle 2 at distance r_{12}. Ornstein and Zernike proposed to divide $h(r_{12})$ into direct part and indirect part. $c(r_{12})$ is the direct correlation function that describes direct influence that particle 1 has on particle 2, irrespective other particles. $h(r_{12}) - c(r_{12})$ is the indirect part that describes the influence that particle 1 asserts on particle 3, which in turn affects particle 2. The indirect effect is

weighed by the density and integrated over all the possible position of particle 3, $\boldsymbol{r_3}$**.** Based on the decomposition of $h(r_{12})$, we can write equation, [26]

$$h(r_{12}) = c(r_{12}) + \rho \int c(r_{13})h(r_{23})d\boldsymbol{r_3} \quad (27)$$

Eq.27 is called the Ornstein-Zernike equation. In order to solve Eq.27, the direct correlation function $c(r_{12})$ must be written in terms of $g(r)$ or $h(r_{12})$, so that $h(r_{12})$ can be evaluated in a closed integral equation. The equation that gives $c(r)$ in terms of $g(r)$ or $h(r_{12})$ is called 'Closure'. Like what we have discussed, r_{12} is the relative center to center distance between two particles and we will start to use r in the following sections instead.

3.2 Solve Ornstein-Zernike Equation Using MPB-RMSA Closure with Hard Sphere Yukawa Potential (HSY).

In our solution, L62 block copolymer forms mixed micelles with AOT surfactant in water. AOT sulfonate headgroups cause the mixed micelles to be charged and become macroions. In our macroion solution, counterions and solvent molecules constitute the uniform neutralizing background and screen the potential between macroions. The static structure properties of the system are determined mainly by Coulomb repulsive potential since the attractive part of the Derjaguin-Landau-Verwey-Overbeek (DLVO) potential is negligible.[28] The macroions are elongate spherical shaped micelles with hard core and the pair potential is equivalent to Hard-sphere potential. Hence, the structure factor S(q) can be calculated by solving Ornstein-Zernike Equation with the Modified Penetrating microion background corrected rescaled MSA (MPB-RMSA) closure and Hard-sphere Yukawa potential closure (HSY).

MPB-RMSA takes the advantage of the simplicity of Mean sphere approximation closure (MSA) scheme, while performing parameter scaling and correction to improve the MSA

performance in dilute and strongly repulsive colloidal system, which will be discussed later. Right now, let's focus on the MSA closure,[29]

$$\begin{cases} c(x) = -\beta U(x), \ x = r/\sigma > 1 \\ h(x) = -1, \ x = r/\sigma < 1 \end{cases} \tag{28}$$

where r is the center to center distance between two particles, σ is the particle diameter, and $U(x)$ is the pair interaction potential. When the sample solution is dilute, we can let concentration $n = 0$, and we can approximate $h(x)$ based on Eq.27 and Eq.28,

$$h(x) \approx c(x) = -\beta U(x) = g(x) - 1 \tag{29}$$

$$g(x) = 1 - \ \beta U(x), \ x = \frac{r}{\sigma} > 1 \tag{30}$$

Now, the Ornstein-Zernike equation in Eq.27 can be written as,[30]

$$h(x) = c(r_{12}) + n\sigma^3 \int h(|\boldsymbol{r_{12}} - \boldsymbol{r_{13}}|)c(|\boldsymbol{r_{13}}|)d\boldsymbol{r_{13}} \tag{31}$$

where $r_{12} = |\boldsymbol{r_{12}}|$ is the absolute value of the relative distance between particle 1 and particle 2. $\boldsymbol{r_{ij}} = \boldsymbol{r_i} - \boldsymbol{r_j}$ is the distance vector between particle i and j. n is the number density of the system. Ornstein-Zernike equation in Eq.31 can be solved with MSA closure, Eq.28 combining with the Hard-sphere Yukawa potential (HSY).

In the HSY model, $U(r)$ is Coulomb repulsion between a pair of charged spherical particles. Pair potential in HSY model is described as, [29]

$$\beta U(x) = \begin{cases} \infty, \ \ x = \frac{r}{\sigma} < 1, \\ \gamma \frac{e^{-kx}}{x}, \quad x > 1, \end{cases} \tag{32}$$

γ is a dimensionless coupling parameter and k is the screening parameter. Eq.32 reflects that particle contact and interpenetration are unphysical. Based on the DLVO theory, the coupling parameter γ which describes mutual interaction of electric double layers of 2 particles is denoted as,

$$\gamma = \frac{L_B}{\sigma}\left(\frac{e^{\frac{k}{2}}}{1+\frac{k}{2}}\right)^2 Z^2 \tag{33}$$

L_B is the Bjerrum length, Z is the effective charge number in the unit of elementary charge e and screening parameter k is defined as,

$$k^2 = \frac{\frac{L_B}{\sigma}}{1-\phi}(24\phi|Z| + 8\pi n\sigma^3), \tag{34}$$

Use Eq.28 and Eq.31, we can solve for the direct correlation function $c(x)$,[9]

$$\begin{cases} c(x) = A + Bx + \frac{1}{2}\eta A x^3 + \frac{Csinh(kx)}{x} + \frac{F(\cosh(kx)-1)}{x}, x < 1 \\ c(x) = -\frac{\gamma e^{-kx}}{x}, x > 1 \end{cases} \tag{35}$$

Where parameters A, B, C, F are defined by Hayter and Penfold.[28] We can then get the static structure factor $S(K = q\sigma)$ by Fourier transform of the Ornstein-Zernicke equation Eq.31 using the direct correlation function Eq.35. The resulting structure factor S(K) is,

$$S(K) = 1/(1 - 24\eta a(K)) \tag{36}$$

η is the volume fraction of micelles, in our experiment. $a(K)$ is

$$\begin{aligned} a(K) = {} & \frac{A(sinK - KcosK)}{K^3} \\ & + \frac{B\left[\left(\frac{2}{K^2} - 1\right)KcosK + 2sinK - \frac{2}{K}\right]}{K^3} \\ & + \frac{\eta A\left[\frac{24}{K^3} + 4\left(1 - \frac{6}{K^2}\right)sinK - \left(1 - \frac{12}{K^2} + \frac{24}{K^4}\right)KcosK\right]}{2K^3} \\ & + C\left(k\,coshk\,sinK - K\,sinhk\,\frac{cosK}{K(K^2 + k^2)}\right) \\ & + \frac{F[k\,sinhk\,sinK - K(coshk\,cosK - 1)]}{K(K^2 + k^2)} + \frac{F(cosK - 1)}{K^2} \\ & - \frac{\gamma e^{-k}(ksinK + KcosK)}{K(K^2 + k^2)} \end{aligned}$$

(37)

The radial distribution function g(x) is then calculated as,

$$g(x) = 1 + 1/12\pi\eta x \int_0^\infty [S(K) - 1]Ksin(Kx)dK \quad (38)$$

The purpose of this section is to show the general steps of calculating $S(q)$ and $g(r)$ with MPB-RMSA and HSY closures and the detailed steps are discussed by Hayter and Penfold.

3.2.1 Modified Penetrating Microion Background Rescaled-MSA (MPB-RMSA)

When the solution is dilute, the pair correlation function is $g(x) = 1 - \beta U(x)$ as shown in Eq.30. When the macroions are strongly repelled in our case, the pair potential energy, $U(x)$, dominates the thermal energy, $1/\beta = kT$. This will make $\beta U(x) > 1$ and will cause radial distribution function $g(x) < 0$, which is unphysical. In the family of strongly repelled particles with HSY potential, hard-core size σ plays no physical role and particles share the same Yukawa tail ($U(r > \sigma)$). Knowing that we can fix the problem of MSA by enlarging the hard-core size σ and volume fraction while keeping the concentration n unchanged, the inflating parameter s $(0 \leq s \leq 1)$ is applied to MSA closure. The value of s is determined by Newton-Raphson type method and the rescaled parameters are physical if they satisfy the Gillan condition $g_{MSA}(x' = 1, \sigma', Z^*, k^*, \gamma^*) = 0, x' = \frac{r}{\sigma'}$ or a different s has to be applied. Gillan condition makes sure that rescaled parameters will not produce a negative $g(r)$ and make sure that there is no particle contact. The rescaled parameters are,

$$\sigma' = \sigma/s \quad (39)$$

$$\gamma' = \gamma_{mod}s \quad (40)$$

$$k' = k_{mod}/s \tag{41}$$

$$\phi' = \phi/s^3 \tag{42}$$

The subscript 'mod' indicates the parameter is modified. We will discuss these modifications shortly. In our colloidal solution, there are ions that are uniformly distributed in the background and no spacial correlations among them. Ions in the solution ensure the electroneutrality and screen the interaction potential between charged colloidal particles.[28] For a given colloidal system with volume fraction ϕ, under the assumption that the ion background is completely uniform, there is fraction ϕ of ions that penetrate the colloidal hard core, which reduces the charge of particle from Z to $Z(1-\phi)$.[29]

In dilute solution, if the repulsion among macroions is weak, the reduction of the charge is sometime negligibly small, so it is not necessary to take this effect into account. In our case, however, the Yukawa repulsion is strong, and the parameter rescaling will produce a large effective volume fraction ϕ'. As a result, the charge reduction is not negligible anymore. Therefore, during the rescaling process of MSA, we must apply the Penetrating Microion Background (PB) correction and increase the Z to Z^*,

$$Z^* = Z/(1-\phi'), \tag{43}$$

And change γ to γ^*, and k to k^*,

$$\gamma^* = \gamma'/(1-\phi')^2 \tag{44}$$

$$k^* = k' - 2\phi'^{\frac{1}{3}}\log(1-\phi'), \tag{45}$$

From Eq.34, the $1/(1-\phi)$ term corrects the free volume accessible for microions of screening parameter k. A problem rises after we plug Z^* into Eq.34 and effectively double the correction to the screen parameter k. To correct this double correction of k, a modified k is used,

$$k_{mod} = k\sqrt{1-\phi} \tag{46}$$

$$\gamma_{mod} = \gamma(k_{mod}) = \gamma e^{(k_{mod}-k)} \left(\frac{1+\frac{k}{2}}{1+\frac{k_{mod}}{2}} \right)^2 \tag{47}$$

The modified PB-RMSA (MPB-RMSA) uses original analyticity of MSA closure with modified parameters; $g_{MPB-RMSA}(r) = g_{MSA}(\sigma', Z^*, \gamma^*, k^*)$. MRB-RMSA closure gives reliable approximation of $g(r)$ even at highly charged colloidal system, where the traditional Rescaled-MSA (RMSA) closure tends to underestimate the principal peaks of $g(r)$ and $S(q)$.[29,31] We tested our MPB-RMSA code by successfully reproducing the $S_{MPB-RMSA}(q)$ and $g_{MPB-RMSA}(x)$ curves from a previous study [29] using parameters; effective charge $Z = 100$, Bjerrum length $L_B = 5.62nm$, hard sphere diameter $\sigma = 200nm$ and four volume fractions $\phi = 0.0005, 0.005, 0.055, 0.105$. Additionally, the RMSA model is also plotted against the MPB-RMSA model using same parameter values, as shown in figure 1.

In Fig.3.1, we can clearly see that RMSA model underestimates the principal peaks of $S(q)$ and $g(x)$, whereas MPB-RMSA captures them correctly. In our system, the sample solution is dilute (5 wt.%) and interactions between particles are strong due to the active micellar charge binding process with increasing temperatures. Considering the fact that Mean Sphere approximation (MSA) fails at dilute solution, strong interparticle repulsion condition and RMSA model underestimates the interaction potential[29], we decided to apply a more involved model to estimate the structure factor in our micelle system: Modified penetrating background corrected rescaled mean sphere approximation (MPB-RMSA).

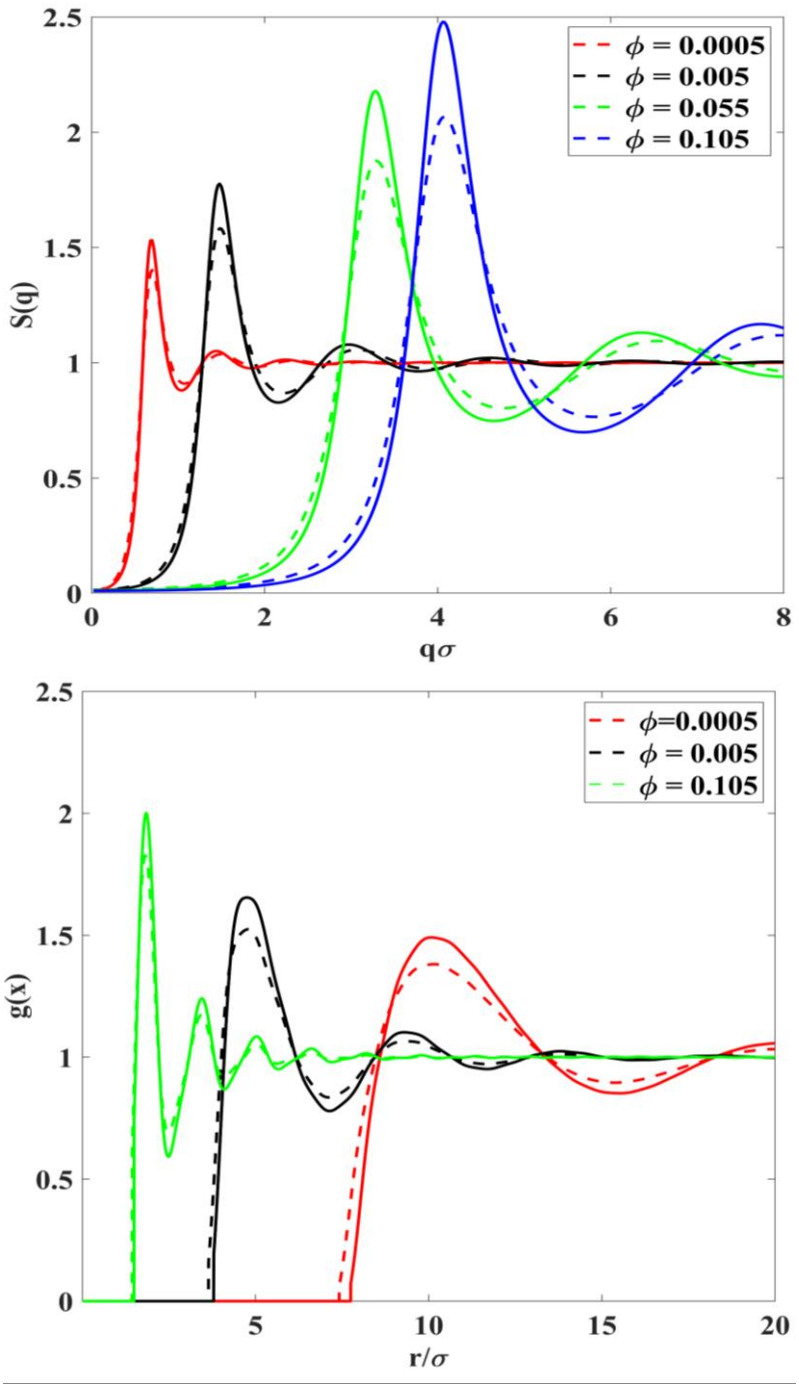

Fig.3.1 The Upper figure is static structure factor $S(q)$ plot versus $q^* \sigma$. The lower figure is radial distribution function $g(x = r/\sigma)$ plot versus $x = r/\sigma$. In both figures, The MPB-RMSA model is potted in solid line and RMSA model is plotted in dotted line. The parameters used for plotting are: $Z = 100$, $\sigma = 200nm$, $Lb = 5.62nm$. The salt concentration is 0.

CHAPTER 4. Introduction to Scattering Experiments

4.1 Scattering Experiment Setup

Fig.4.1 shows the top view of a typical light scattering experiment set up. Vertically polarized radiation incidents on the micelle. After the incident radiation passes through, some is scattered. The detector is placed at the scattering angle θ and the intensity $I(\theta, t)$ is measured at θ and time t. In our case, the scattering medium is made up of water molecules and micelles. In scattering medium, the volume that is illuminated by the incoming radiation is called the 'scattering volume' V. Scattering is caused by the variations density of the medium that in turn causes the variation of dielectric constant of the medium.[32] For example, a micelle scatters the incident radiation when because its index of refraction is different from the index of refraction of the water it is dispersed in.

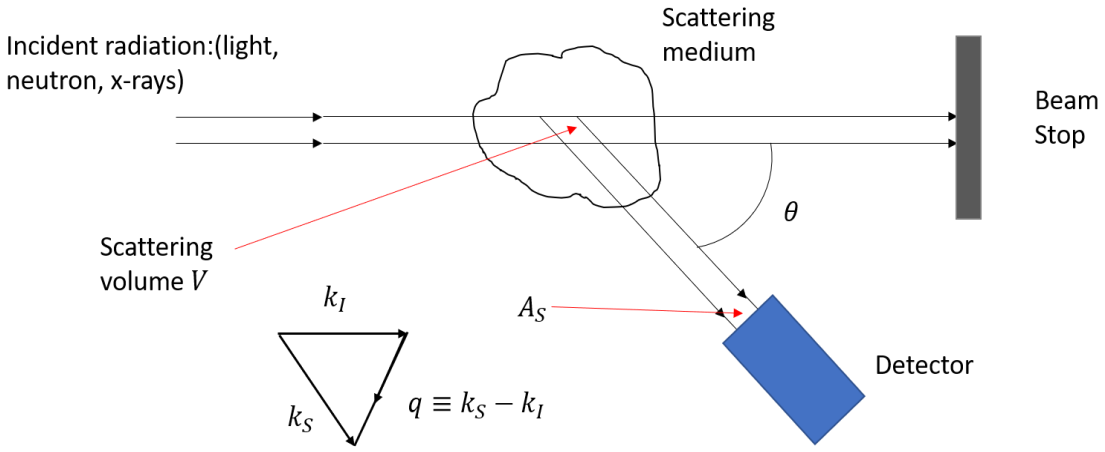

Fig.4.1 Top view of a scattering experiment set up. A plane wave travel through the scattering volume V and some is scattered and is detected by the detector plane area A_S at angle θ respect to the transmitted radiation that is stopped at beam stop, $\vec{q}$ is the scattering vector.

There are mainly two types of scattering experiments, each of them can provide distinct information about the scattering medium. In the first type of experiment, the scattering intensity is measured at various scattering angle θ and is averaged over time. This type of scattering experiment is called 'static scattering', which provides information about the shape of the particles and about the averaged spatial arrangement among them.

In the second type of experiment, the dependence of scattering intensity over time t is monitored at one scattering angle θ. This type of scattering is called 'dynamic scattering' and it yields information about particle dynamics; how the particles participate Brownian motion and how the shape, relative density and configuration of the medium change over time.[33]

In a scattering experiment (neutron, light, etc.), an incident wave creates a field and its strength is expressed as[34],

$$E_I(r,t) \equiv E_0 e^{i(k_I r - \omega t)} \quad (1)$$

k_I is the propagating vector of the incident radiation and has magnitude $|k_I| = \frac{2\pi}{\lambda} = k$, where λ is the wavelength of the radiation and ω is the angular frequency.

In a scattering event, we assume that first, the scattering is weak so that large fraction of incident radiation is undeviated and the electromagnetic field is same in the scattering medium compared to the one of the incident waves. Second, we assume that the particles and solvent molecule does not absorb the radiation. Third, we assume that the scattering events are elastic, so that the change of the wavelength and frequency of the scattered radiation is negligible.[15] Therefore, the magnitude of the scattered wave k_S vector is also $\frac{2\pi}{\lambda}$ as k_I does.

The amplitude of the scattered radiation $E_S(R,t)$ to a point detector at the far field can then be written

$$E_S(R,t) = -\frac{k^2 E_0}{4\pi}\frac{\exp[i(kR-\omega t)]}{R}\int_V \left[\frac{\varepsilon(r,t)-\varepsilon_0}{\varepsilon_0}\right]\exp(-iq*r)\,d^3r \qquad (2)$$

where ε_0 is the dielectric constant of the medium, V is the scattering volume and $\varepsilon(r,t)$ is the local dielectric constant of the scattering medium at the position r and time t. $\vec{q}$ is the scattering vector and is defined as, as shown in Fig.4.2

$$\vec{q} \equiv k_S - k_I \qquad (3)$$

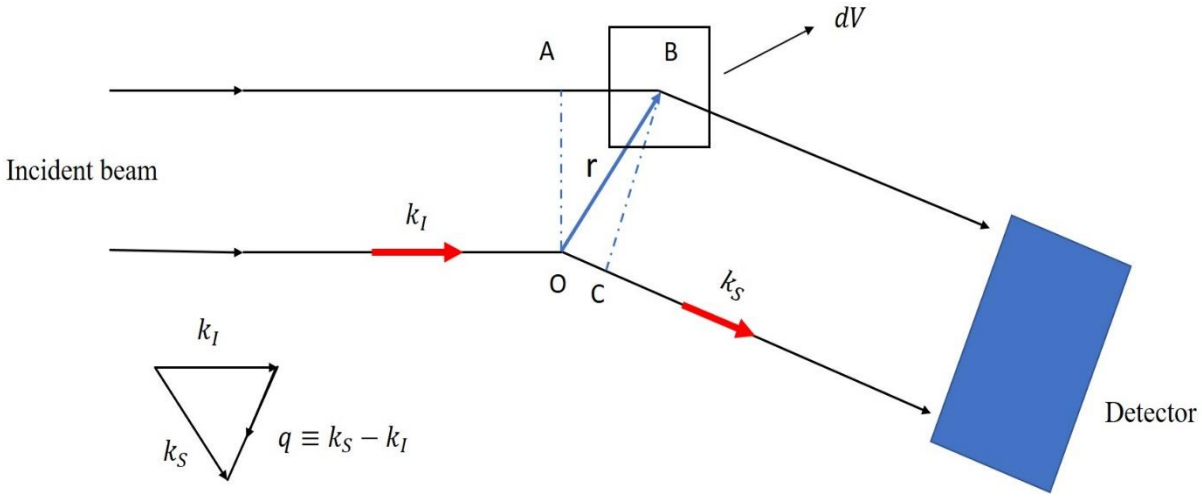

Fig.4.2 Is the zoomed in version of Fig.1 and it shows the difference between the traveled distance of the bottom wave, which goes through origin O in scattering volume V, and top wave through the scattering volume dV at position r.

The first part of the Eq.2 represents the dipole induced by the incident radiation at position r in volume dV has amplitude proportional to that of the incident wave, E_0. The term $\varepsilon(r,t)$ in Eq.2 explains that scattering is caused by the density fluctuation of the medium; if the scattering medium is homogenous everywhere, $\varepsilon(r,t) = \varepsilon_0$ and scattering will not take place. The last part of Eq.2 corresponding to the phase shift resulting from the

different travel distance of the top and bottom wave shown in Fig.4.2. The phase difference $\Delta\phi$ between the two waves that travels through point B and point O is,

$$\Delta\phi = \frac{2\pi}{\lambda}(k_I r - k_S r) = -2\pi s \cdot r = -q \cdot r \quad (4)$$

where s is defined as

$$|s| = |(k_S - k_I)/\lambda| = \frac{2sin\theta/2}{\lambda} \quad (5)$$

λ is the wavelength of the incident wave. Plugging Eq.5 into Eq.4, we have the accurate expression for the scattering vector $\vec{q}$ as,

$$\vec{q} = \frac{4\pi sin\theta}{\lambda} \quad (6)$$

4.1.1 Small Angle Neutron Scattering (SANS)

Small angle neutron scattering (SANS) is one way to utilize both scattering techniques we mentioned in the previous section. We choose to use this method to probe Pluronic L62, Aerosol-OT (AOT) mixed micelles structure dispersed in the D_2o solvent with neutrons beam. The advantage of SANS is that it allows us to probe the scattering medium on the angstrom scale (Å), so that the physical properties of the whole sample can be known. Further, the SANS approach is non-invasive, so the result is more accurate compared to others.

Fig.4.3 shows the typical setup of the small angle neutron scattering experiment (SANS). The beam of neutrons that have been selected by velocity will pass the beam selector and impinge on the sample. Consequently, some of the neutron beam will be scattered by θ angle and reach the detector plane with area A_d. The momentum transfer $\vec{q} \equiv k_S - k_I$ is defined as before. In SANS experiment, studying structural property of

particles suspended in the solvent is our major interest. Therefore, the scattering of neutrons that caused by the difference between particles material density and solvent density should be reflected in Eq.2. It is also noteworthy that, in SANS, the amplitude of the scattering detected at a point on the detector comes from multiple particles. Therefore, we need to generalize Eq.2 to account for multi-particle scattering.

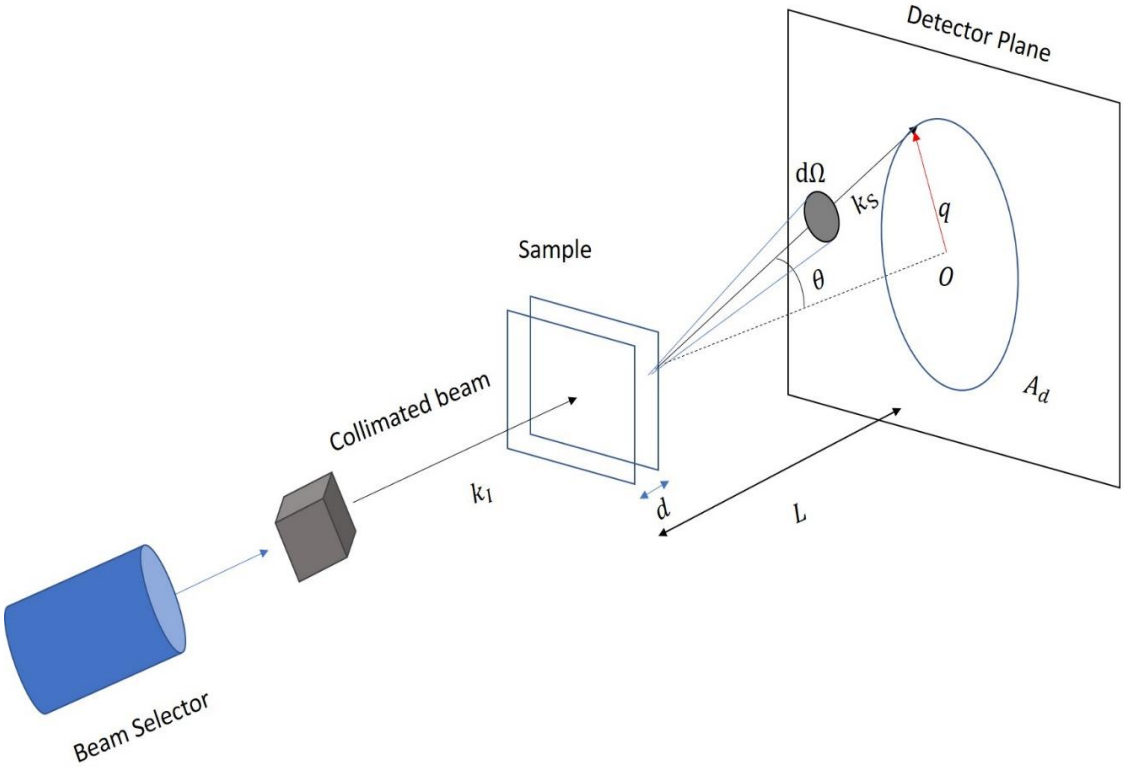

Fig.4.3 The schematics of a typical Small Angle Neutron Scattering (SANS) is shown. The beam selector will let the selected neutron beam pass through based on the beam velocity and the sample scatters the neutron beam into 2θ angle on the detector plane with area A_d.

4.1.2 Discrete Scatters

In the many particle system, we have N particles in the scattering volume V and the scattering amplitude is contributed from multiple particles, whose position of center of mass at time t is described by $\{R_j(t)\}$, and the position of dV in each particle is denoted by $\{r_j(t)\}$ as shown in Fig.4.4. The choice of the origin O can be a point on the scattering medium or in the solvent.

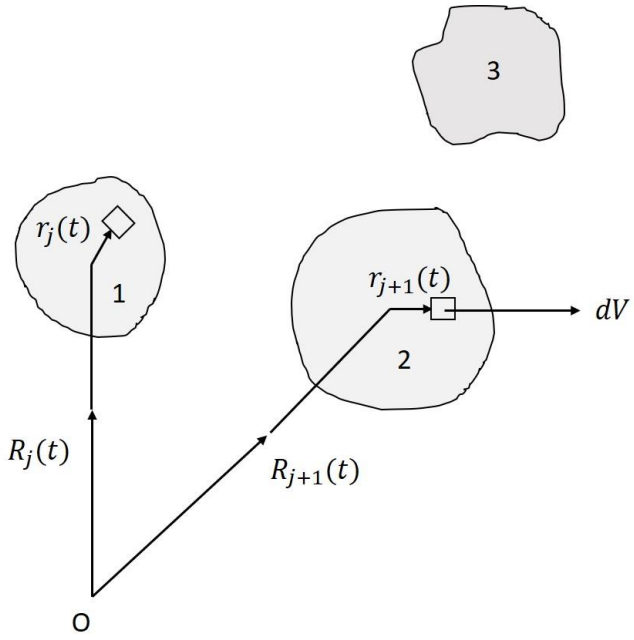

Fig.4.4 In a three-particle system, the position vector of discrete scatters $\{R_j(t)\}$ and the position of the unit volume dV respect to the center of the mass $\{r_j(t)\}$ at time t. There is a spatial correlation between particle 1 and 2, whereas in the dilute situation, there is no correlation between particle 1 and 3 when particle 2 is missing.

The term in Eq.2, $\varepsilon(r,t)-\varepsilon_0$ can be expanded as[35],

$$\varepsilon(r,t)-\varepsilon_0=\varepsilon_P(r,t)-\varepsilon_S \quad \text{(inside any particles)}$$
$$+\varepsilon_S(r,t)-\varepsilon_S \quad \text{(outside any particles)}$$
$$+\varepsilon_S-\varepsilon_0 \qquad \text{(anywhere in Volume V)} \tag{7}$$

In Eq.7, $\varepsilon_{P(S)}(r,t)$ is the dielectric constant of particles (or solvent) at position r and time t. ε_S is the average dielectric constant of solvent and ε_0 is the average dielectric of the medium. When we plug Eq.7 back into Eq.2, we have 3 contributions in the scattering amplitude. The first contribution is from the scattering of the particle, which is due to the difference between particles' dielectric constant and solvent's dielectric constant. Second contribution comes from the density fluctuation of the solvent, which is very small and negligible. Third contribution does not have spatial dependence. The amplitude reflects the scattering from the whole sample volume V, which can be neglected.

Based on the Fig.8, Eq.2 can be rewritten as,

$$E_S(R,t)=-\frac{k^2E_0}{4\pi}\frac{\exp[i(kR-\omega t)]}{R}\times$$
$$\sum_j\left[\int_V\left[\frac{\varepsilon_P(r,t)-\varepsilon_S}{\varepsilon_0}\right]\exp(-iq*r)\,d^3r\right]\exp\left(-iq*R_j(t)\right) \tag{8}$$

In Eq.8 the amplitude of the wave scattered from the j^{th} particle is proportional to E_0. Term $e^{-iqR_j(t)}$ accounts for the phase shifts caused by different particles' positions. Furthermore, the permittivity terms in Eq.8 tells the scattering density fluctuation between solute (scattering medium) and solvent molecules. In the SANS experiment, the time averaged intensity is studied, thus Eq.8 can be simplified as,

$$E_S(R,t)=-E_0\frac{\exp[i(kR-\omega t)]}{R}$$
$$\times\sum_j\left[\int_V\Delta\rho(r_j,t)\exp(-iq*r)\,d^3r\right]\exp\left(-iq*R_j(t)\right) \tag{9}$$

Where the term $\Delta\rho(r_j, t) = \frac{k^2}{4\pi}\frac{\varepsilon_P(r,t)-\varepsilon_S}{\varepsilon_0}$ represents the scattering density between particle and solvent molecules. In SANS, neutron counts are detected on the detector plane with area A_d and time averaged absolute intensity per unit area, $I(q)$, is calculated from the scattering intensity detected at a point in the far field $I_S(q) = \langle|E_S(R,t)|^2\rangle$ as $\frac{d\Sigma}{d\Omega} = \frac{\langle I_S(q)\rangle A_d R^2}{E_0^2 A_d V}$.[36] The numerator of the previous expression is a measure of the scattered intensity per unit time and the denominator is the product of incident flux and the detection solid angle, so $\frac{d\Sigma}{d\Omega}$ can be seen as the 'differential scattering cross section area per unit sample volume V',

$$\frac{d\Sigma}{d\Omega} = V^{-1}\left\langle\sum_{j=1}^{N}\sum_{i=1}^{N}\langle F_j(q)F_i^*(q)\rangle \exp\left[-iq\left(R_j - R_i\right)\right]\right\rangle \tag{10}$$

where $F_j(q) = \int_V \Delta\rho(r_j)\exp(-iq*r)\,d^3r$ is the time averaged scattering intensity of a single particle. $\langle F_j(q)F_i^*(q)\rangle$ represents the scattering amplitude averaged over the particle size distribution and orientations, which can be decomposed as[16],

$$\langle F_j(q)F_i^*(q)\rangle = [\langle|F(q)|^2\rangle - \langle|F(q)|\rangle^2]\delta_{ij} + \langle|F(q)|\rangle^2 \tag{11}$$

Plug Eq.11 back into Eq.10 and after simplification we have,

$$\frac{d\Sigma}{d\Omega} = n_P[\langle|F(q)|^2\rangle - \langle|F(q)|\rangle^2] + n_P|\langle F(q)\rangle|^2 S(q) \tag{12}$$

where $n_p = \frac{N_P}{V}$ is the average number density of the particle in the sample volume V. $S(q)$ is the static interparticle structure factor denoted as,

$$S(q) = N_P^{-1}\left\langle\sum_{j=1}^{N}\sum_{i=1}^{N}\exp\left[-iq\left(R_j - R_i\right)\right\rangle\right. \tag{13}$$

In dilute solution, particles are widely separated from each other and their behaviors are uncorrelated, as shown in Fig. 4.4, the cross term, $i \neq j$, in Eq.13 vanishes, so the structural factor $S(q) = 1$. On the contrary, in concentrated solution, where particles are spacial correlated, the value of $S(q)$ must be determined. After rearrangement of Eq.12, we can write the absolute intensity $I(q)$ as,

$$\frac{d\Sigma}{d\Omega} = n_P P(q) S'(q) \tag{14}$$

The terms are defined as

$$S'(q) = 1 + \beta(q)(S(q) - 1) \tag{15}$$

$$\beta(q) = |\langle F(q) \rangle|^2 / \langle |F(q)|^2 \rangle \tag{16}$$

Omitting the prefactors, the form factor $P(q) \equiv \langle |F(q)|^2 \rangle$. $S'(q)$ is an apparent interparticle structural factor. $\beta(q)$ $(0 \leq \beta \leq 1)$ is the q dependent factor that suppresses the oscillation of the true structure factor $S(q)$.[16] $\beta(q)$ corrects the $S(q)$ in the event of scattering from polydisperse or non-spherical particle system, such as our system of elliptical L62/AOT particles. In the case of monodisperse spherical particle solution, $\beta(q) = 1$ and the absolute intensity reduces to $\frac{d\Sigma}{d\Omega} = n_p P(q) S(q)$.

The interparticle structure factor, $S(q)$, can be related to the radial distribution function $g(r)$, which describes the possibility of finding any particle at a distance r away from the given particle. In a N particle system with volume V, $(N/V)g(R)dV$ represents the number of particles in dV at a distance R from the center of a given particle. The structure factor is written as[37]

$$S(q) = 1 + 4\pi n_P \int_0^\infty \frac{(g(r)-1)R^2 sinqR}{qR} dR \tag{17}$$

The inverse Fourier transform of Eq.17 gives the radial distribution function $g(R)$ in terms of $S(q)$,

$$g(R) = 1 + \frac{1}{2\pi^2 n_p}\int_0^\infty (S(q) - 1)q^2 \frac{sinqR}{qR} dq \tag{18}$$

A detailed discussion about the structure factors and radial distribution functions used in our experiment has been given in the previous chapter. In Fig.5, the peak of the radial distribution function $g(r)$ represents the likely distance to the nearest neighbor of particles.

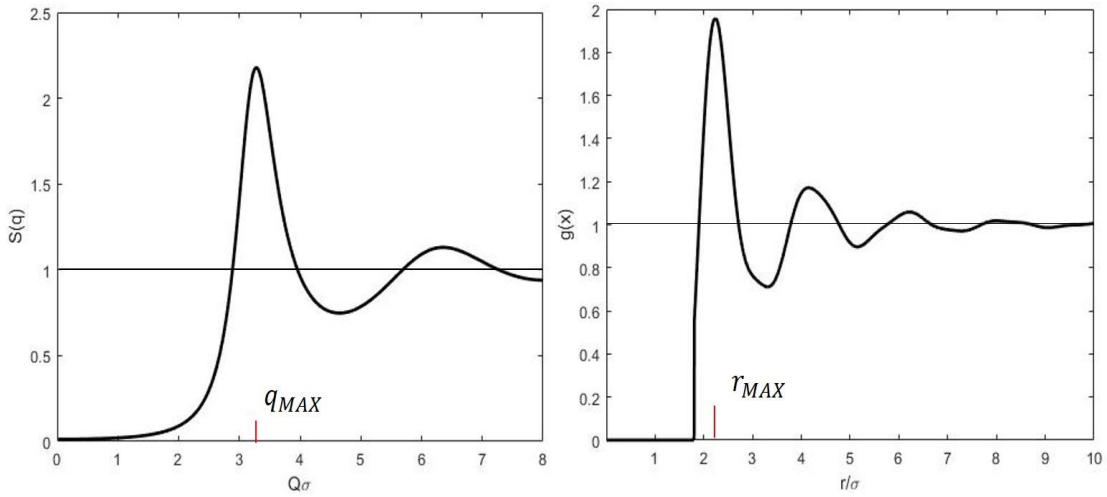

Fig.4.5 Modified Penetrating background Rescaled-MSA (MPB-RMSA) structure factor S(q) plot against $q\sigma$ and the corresponding radial distribution function $g(r)$ plot against r/σ

$g(r)$ has a value of 0 when the interparticle separation is smaller than the particle diameter σ, since two particles can not occupy the same position at the same time. The peak position in the structure factor $S(q)$ describes the mean nearest neighbor interparticle separation distance, similar to the Bragg reflection. The value of q_{MAX} and r_{MAX} are usually related by the 'Bragg condition' $q_{MAX}r_{MAX} \approx 2\pi$, as shown in Fig.45.

4.2 Initial Data Reduction

In the Small Angle Neutron Scattering (SANS) experiment, the detector receives scattered radiation that contains structural information about the sample. In our experiments, the micelle solution is contained in the sample cell that is targeted for scattering. The intensity of the scattered radiation is attenuated by the effect of the sample cell and by the smearing effect of limited instrumental resolution. As a result, we must perform background scattering measurements in addition to the experiment, so that the coherent sample scattering intensity can be extracted from the mixed scattering intensity received by the detector. A complete SANS experiment includes measurements of the scattering intensity of an empty sample cell, of sample back ground solutions, and a complete set of transmission measurements; the transmission of an empty cell, a reference sample, a standard sample and the direct beam.

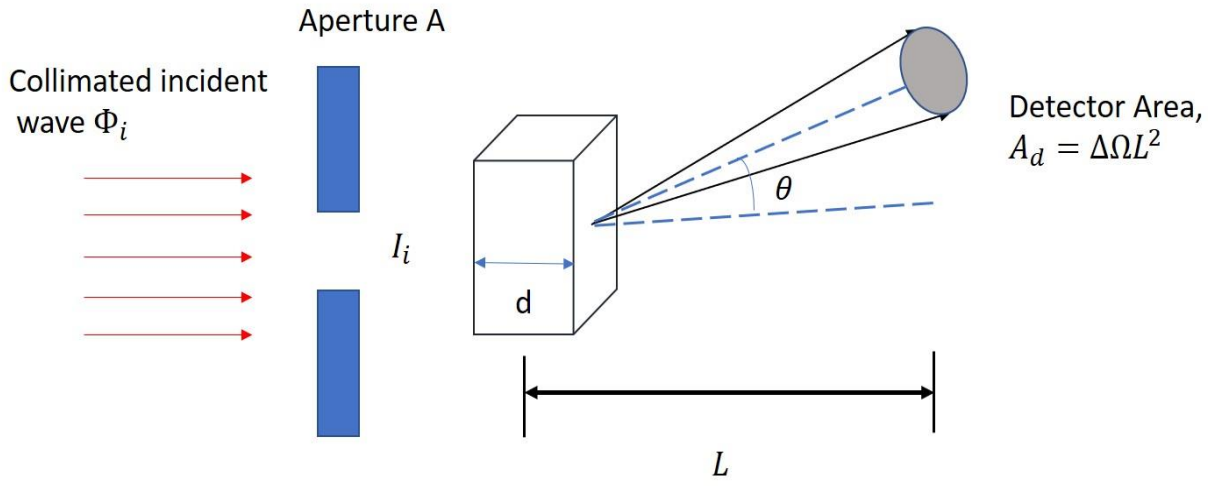

Fig.4.6. Schematic of the simplified neutron scattering set up. Collimated wave with intensity I_i and flux ϕ_i; Aperture area A. Sample thickness d and solid angle $d\Omega$. Detector plane area A_d placed at distance L respect to sample with efficiency $E(\lambda) < 1$.

The general layout for a neutron scattering experiment is shown in Fig.4.6; Collimated incident neutrons with flux ϕ_i pass through an aperture with area A. The incident neutron waves impinge on a sample with width d and get scattered into the solid angle $d\Omega$. The scattered wave is then detected on the detector plane area A_d placed at distance L with respect to the sample. The detected incident intensity per second I_i can be expressed by the incident flux Φ_i and aperture area A with detector efficiency $E(\lambda) < 1$ as[38],

$$I_i = \Phi_i(\lambda) A E(\lambda) \tag{1}$$

The incident beam that passes the aperture will interact with sample at position x ($0 \leq x \leq d(sample\ thickness)$) and the incident radiation will be attenuated by a factor of $e^{-\mu x}$. After scattering, the intensity if the beam is further attenuated by a factor of $e^{-\mu(d-x)}/cos\theta$, and the radiation is finally scattered into a solid angle $\Delta\Omega$ and received at the detector plane. The background corrected scattered radiation measured at scattering angle θ can be written as the integral[38],

$$I(\theta) = \int_0^d \phi_x\, AE\Delta\Omega\, e^{-\mu x} \frac{e^{-\mu(d-x)}}{\cos\theta} \frac{d\sigma}{d\Omega} \rho\, dx \tag{2}$$

In small angle neutron scattering (SANS), $\cos\theta \approx 1$ and the integral can be calculated as,

$$\begin{aligned} I(\theta) &= \Phi_i A\ \Delta\Omega\ \mathrm{E}\ d\ e^{-\mu d} \frac{d\Sigma}{d\Omega} \\ &= \Phi_i A\ \Delta\Omega\ \mathrm{E}\ d\ T_s \frac{d\Sigma}{d\Omega} \\ &= C(\lambda) d T_s \frac{d\Sigma}{d\Omega} \end{aligned} \tag{3}$$

$\rho(cm^{-3})$ is the number density of the scatters. $T_s = e^{-\mu d}$ is the transmission rate, where $\mu(cm^{-1})$ is the attenuation factor and $1/\mu\ (cm)$ is the mean free path of the wave that describes the wave travel distance before scattering happens. $C(\lambda)$ is called the instrument

parameter and is defined by the experiment set up itself; aperture size, detector efficiency, sample-detector distance and solid angle $\Delta\Omega$.[39] In reality, the instrument resolution is not definite; the wavelength has a distribution of $\frac{\Delta\lambda}{\lambda}$, the incident radiation has finite divergence and the aperture has finite size. Under this circumstance, the instrumental resolution effect must be considered by incorporating smearing effects into the intensity fitting model when we perform data analysis. A detailed discussion of data smearing will be given later.

4.2.1 Transmission

In Eq.3, the transmission rate T_s is defined as the ratio between the transmitted radiation to the incident radiation at $\theta = 0$, as shown in the Fig.1 below,

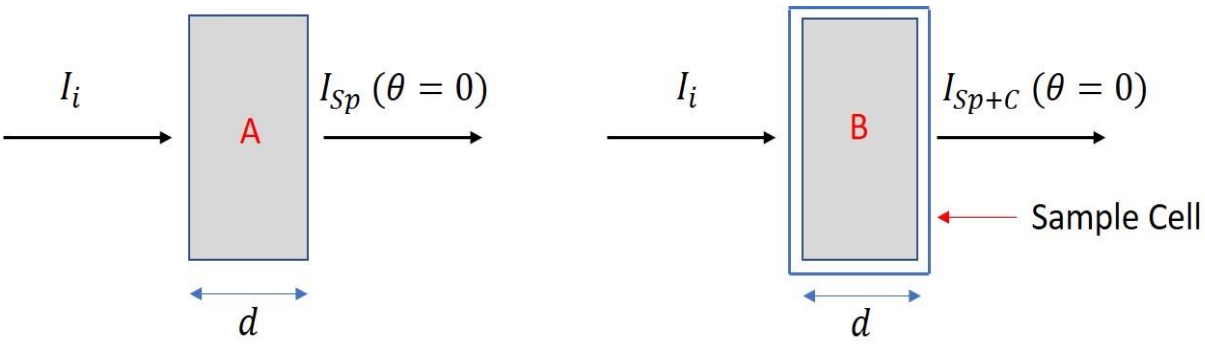

Fig.4.7. Schematic of the transmission measurements of pure sample (A) and the transmission measurements of sample in the sample cell (B) at scattering angle $\theta = 0$.

The transmission rate $T_s = e^{-\mu x}$ is based on the transmission measurement of the pure sample with width d, as shown in Fig.4.7(A). However, in our SANS experiment, the sample is contained in a cell that yields an extra attenuation to the radiation received at the

detector plane, as shown in Fig.4.7(B). As the result, the background correction to the detected radiation is critical.

4.2.2 Background Measurement

In the SANS experiment, the sources of the background scattering can be categorized as either external or internal. The external background consists primarily the electronic noise, sample cell, etc. The internal background originates from the sample itself such as, impurity or solvent molecules in the sample solution.

4.2.3 External Background

In our experiment, the polymer micelles are dissolved in the deuterated water that is contained in a quartz glass sample cell. The front window and back windows of the sample cell will induce extra attenuation of the radiation intensity that will be received at the detector plane, A_d. Therefore, the measurement of the empty container I_C^M is necessary. Further, natural radiation exists in the room, which can be measured with a sheet of cadmium (blocking the neutron beam?) in SANS experiment. In the following paragraphs, we name the measured radiation intensity through the sample and cell as I_{Sp+C}^M, through the empty cell as I_C^M, and with just the room background noise as I_{RM}^M. The transmission rate of the set up shown in Fig.4.7(B) is a little bit different from that of the Fig.4.7(A),[40]

$$T_S = \frac{I_{Sp+C}}{I_c} = \frac{I_{Sp+C}/I_i}{I_c/I_i} = \frac{T_{Sp+C}\ (\theta=0)}{T_C\ \ (\theta=0)} \tag{4}$$

The measured scattering intensity of the sample with cell I_{Sp+C}^{M} contains three parts; 1st the transmitted radiation intensity, 2nd the scattered radiation intensity I_S attenuated by the back window of the cell and 3rd the measured room noise,

$$I_{Sp+C}^{M} = T_{Sp+C} I_S + T_{Sp+C}\, I_C(\theta = 0) + I_{RM}^{M} \tag{5}$$

The measured scattering intensity of the empty cell is defined as the front widow transmitted radiation I_C attenuated by the back-cell window,

$$I_C^{M} = T_C I_C + I_{RM}^{M} \tag{6}$$

Rearranging Eq.6 gives the expression of I_C,

$$I_C = (I_C^{M} - I_{RM}^{M})/T_C \tag{7}$$

Plugging Eq.7 into Eq.5 yields,

$$I_{Sp+C}^{M} = T_{Sp+C} I_S + \frac{T_{Sp+C}}{T_C (I_C^{M} - I_{RM}^{M})} + I_{RM}^{M} \tag{8}$$

After rearranging Eq.8, the scattering intensity I_S of the sample, corrected for the empty sample cell scattering and room background noise can be written as,

$$I_S = \frac{I_{Sp+C}^{M} - I_{RM}^{M}}{T_{Sp+C}} - \frac{I_C^{M} - I_{RM}^{M}}{T_C} \tag{9}$$

Eq.9 is the background corrected sample scattering intensity that can be used by Eq.3 for further instrument resolution correction.

4.2.4 Internal Background

Internal background originates from the sample itself. Impurities, hydrogenous species, or solvent molecules in a concentrated polymer sample solution can result in incoherent scattering. The total differential cross section $\frac{d\Sigma}{d\Omega}$ of the sample scattering is the summation of the coherent and incoherent scattering cross section,[40]

$$\frac{d\Sigma}{d\Omega} = \left(\frac{d\Sigma}{d\Omega}\right)_{coherent} + \left(\frac{d\Sigma}{d\Omega}\right)_{incoherent} \quad (10)$$

Coherent scattering cross section is the q dependent, which represents the interference of the scattered wave from different micelles ($i \neq j$). Therefore, the coherent scattering contains the structural information of the micelles. The incoherent scattering is q independent and it is originated from the inconsistent scattering length of the scatters in the solution. Incoherent scattering is usually a flat background along the q range, and it needs to be subtracted from the total scattering cross section before we analyze the coherent scattering cross section.

4.3 Smearing of the Fitting Model

After scattering data reduction is completed, the output is a 1D SANS data file that contains the information of scattering intensity, mean intensity, standard deviation of intensity, q value, mean q value, $\bar{q}$, standard deviation of q value σ_q and shadow factor f_s (this doesn't seem 1D?). As we mentioned earlier, the precision of the scattering instrument is limited, and this results in a smeared detected intensity. Therefore, to calculate the form and structural factor of the scatters based on the smeared data, we need to smear the intensity model we use. For a SANS experiment, the instrument resolution is approximated with Gaussian distribution and the smeared intensity function is calculated via the nominal scattering vector $\langle q \rangle$, which in our case is $\bar{q}$, [41,42]

$$I_S(\bar{q}) = \int_0^\infty R(q, \bar{q}) I(q) dq \quad (11)$$

$I(q) \equiv n_p P(q) S'(q)$ is the intensity model we used in data analysis that has been discussed in the previous chapter. The Gaussian approximation of the resolution function is defined as,

$$R(q,\bar{q}) \equiv \frac{f_s}{\sqrt{2\pi\sigma_q^2}} e^{\left(\frac{-(q-\bar{q})^2}{2\sigma_q^2}\right)} \tag{12}$$

During the calculating of the resolution function, if $R(\bar{q})$ extends to the negative q value for a given $\bar{q}$ (range of $3\sigma_q$) so we choose to truncate the resolution function at $q = 0$.

CHAPTER 5. RESULT AND DISCUSSION

5.1 Sample Preparation

Pluronic L62 triblock copolymer is received from BASF as a gift, and the deuterated water (D_2O) is purchased from Cambridge Isotope, 99.9% D. Aerosol-OT (AOT) is purchased from Sigma-Aldrich. The solutions are prepared in mass ratio (L62: AOT = 0:100, 25:75, 50:50, 100:0) at 20°C, while the solute is in fixed mass ratio (L62+AOT: D_2O = 5wt.%). To investigate the L62 micellar form and structure factors with various AOT concentrations, SANS experiments were performed SANS instrument at the 40m SANS instrument at the HANARO cold neutron research facility in the Republic of Korea. The measurements were done from 10℃ to 70℃ with increase step of 5℃ by using instrument and neutrons of wavelength λ = 6 Å with the full width half maximum of Δλ/ λ = 12% at two different sample to detector distances (1.16m and 11m) for 40m SANS instrument. The experiment has been repeated under same conditions at Oak Ridge National Laboratory (ORNL) SANS to reassuring the resulting scattering intensity. The details of the chemicals used are summarized in Table 1.

Table 1 Molecular properties of the polymer, solvent.

	Formula	$M_w(g\ mol^{-1})$	SLD($10^{-4}nm^{-2}$)
EO	$(CH_2)_2O$	44	0.566
PO	$(CH_2)_3O$	58	0.343

Table 1 continued

L62	$EO_6PO_{34}EO_6$	2500	0.39
AOT	$C_{20}H_{37}NaO_7S$	434	0.564
D_2O	D_2O	20	6.36

M_w, Molecular weight. SLD, scattering length density (SLD) is calculated using neutron scattering length density calculator provided by NIST center for Neutron Research.

5.2 AOT/L62 100wt%

The SANS result of 5wt% solution of AOT (AOT: L62=100:0) at different temperatures is shown in the fig. 5.1. From scattering intensity plot, it is shown that peak positions satisfy $q_2 = 2 \times q_1$. The equality of $q_2 = 2q_1$ strongly suggests the presence of the lamellar structure (L_α). The third order peaks are also visible for high temperature scattering intensities while they are relatively broad. At low temperatures (10-20°C), lack of higher order peaks and broad peak width suggest that Lamellar structure is not well aligned. As temperature increases scattering peaks become shaper and the correlation between positions of peaks become clearer too. Interestingly, peak positions shift to the higher q range as temperature increases, which implies d spacing of the lamellar structure is decreasing as a function of temperature. This behavior is counter intuitive, considering the expectation of steric interaction. One possible explanation is that the curvature moduli of the lamellar layer decreasing with temperature results in decreasing spacing. This suggests that multi-lamellar vesicles are favored when thermo-stability moves away from planar lamellar structure at high temperatures.[43]

5.3 L62/AOT 100wt%

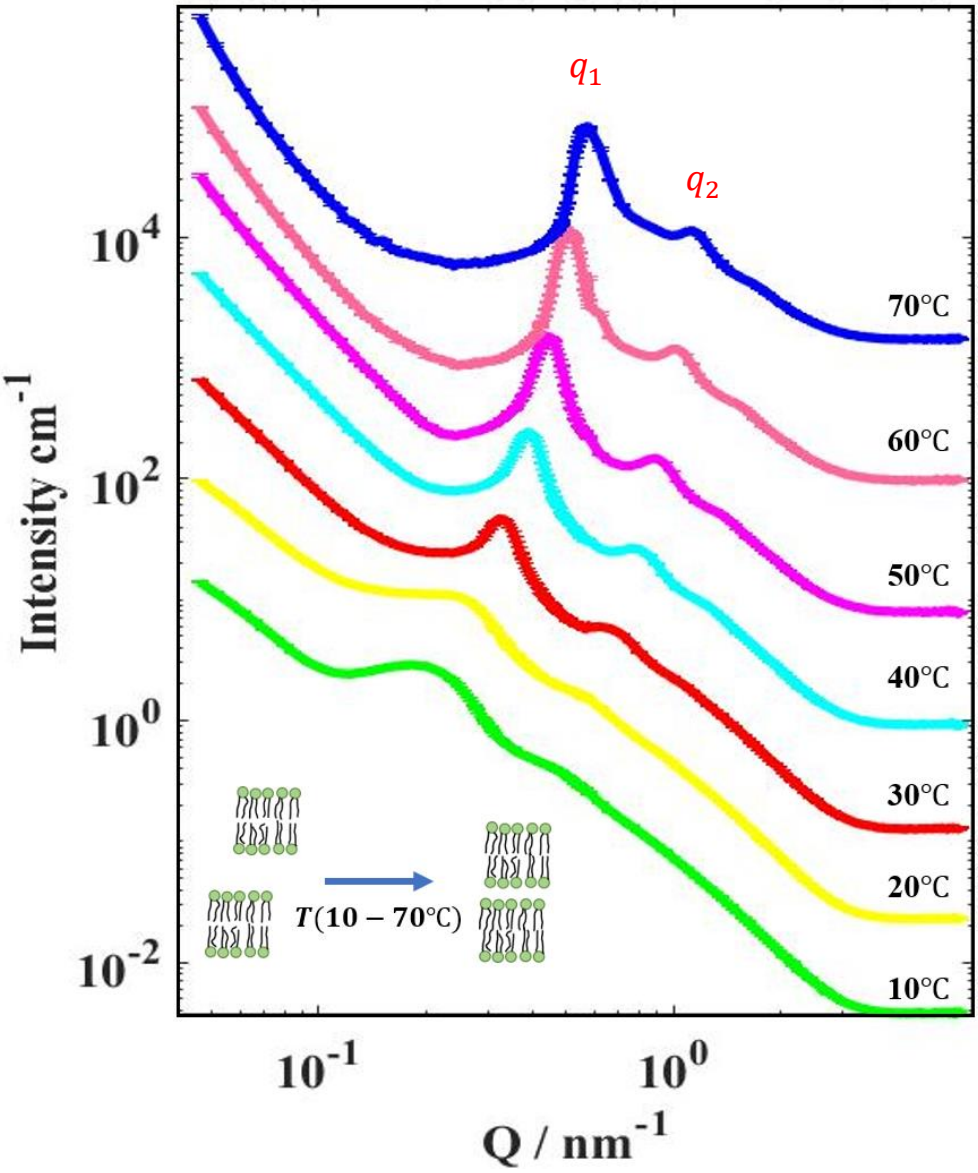

Fig. 5.1 Scattering intensities of 5*wt*%(*AOT*/D_2O) solution at temperature range of 10 -70°*C*. The scattering curves have been shifted vertically for visual clarity. The schematics of AOT lamellar structures from $10-70℃$ is shown in the left corner.

In pure L62 solution (L62: AOT=100:0), Pluronic L62 copolymer exists as Gaussian chains below the room temperature and no micelle structure is observed. (Fig. 5.2**)** The neutron scattering intensity below 30°C is fit as a gaussian chain with excluded volume interaction, which describes individual block copolymer chains in solution with the excluded volume effects. The deviation at low-q values may be due to aggregation of polymer chains at the larger length scales, which is ignored in the current model. From the fit, as temperature increases to 30°C, R_g increases from 1.2 nm to 2.2 nm, which is in good agreement with the literature value of 1.5 nm, the result from a previous SANS experiment[44]. The increasing R_g directly shows that the polymer chain mesh is larger in size at higher temperatures. Such behaviour is reasonable, considering solvent quality at 10°C to 30°C is good for PEO hydrophilic end groups to extend themselves. Also, more polymer chains are participating in the micelle self-assembling process, which results in larger sizes as temperature increases. The changes of in shape of the scattering intensity curves as temperature increasing indicate the transition to the micellar phase. Scattering intensities from 40°C to 60°C have been fitted with Ellipsoid form factors combined with a sticky-sphere structure factor. There are six free parameters to describe the data curves; volume fraction, incoherent background, polar and equatorial radius, perturbation ϵ, and stickiness τ.

From Fig.5.2A, polar radius increases from 3.4 nm at 40°C to 3.5 nm at 60°C. Equatorial radius increases from 7.9 nm at 40°C to 14.5 nm at 50°C and seems to diverge after that. The fitted values have good agreement with previous studies of Pluronics. The increasing

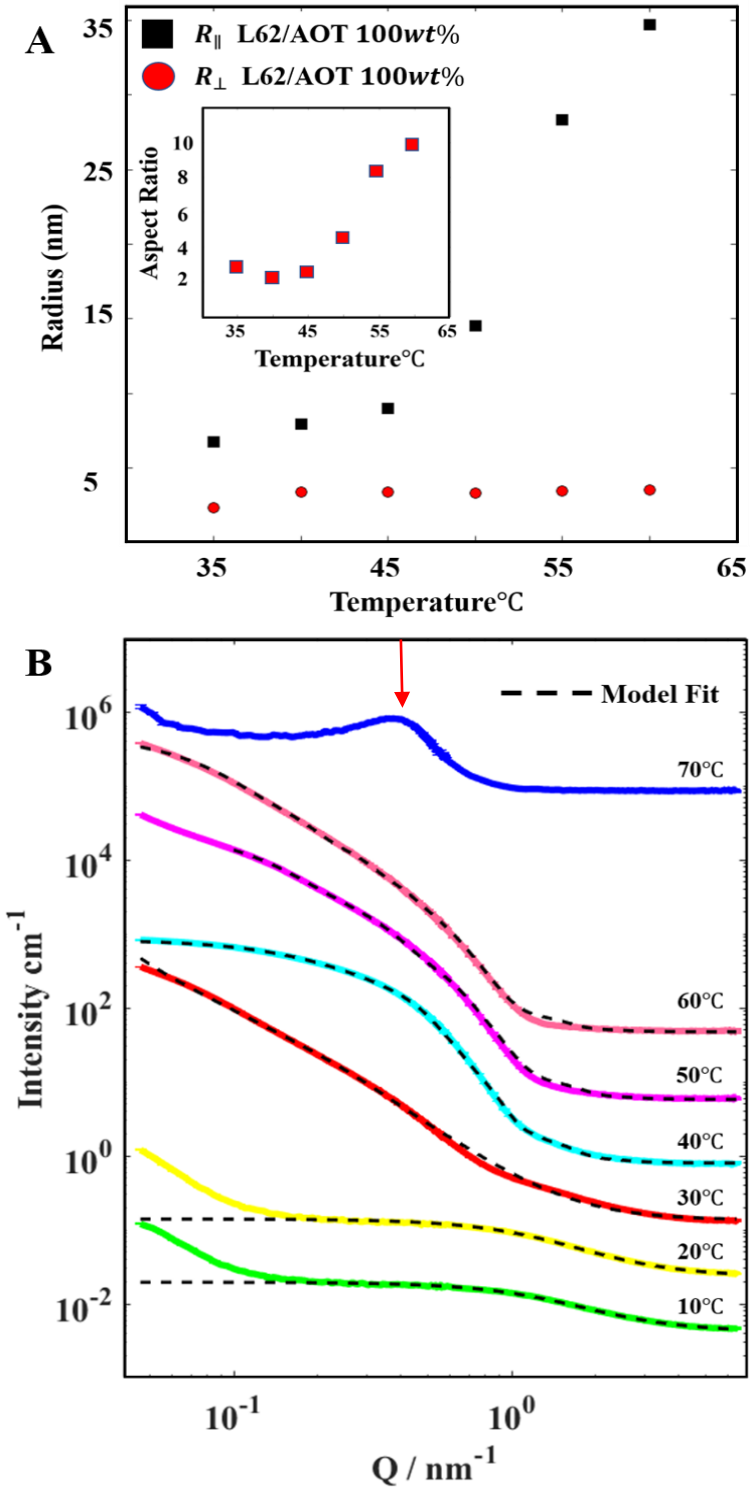

Fig. 5.2(A-B) A. Polar, equatorial radius and aspect ratio of pure L62 micelles. **B**. Scattering intensities of 5wt% **(**L62/D_2O**)** solution at 10 – 70°C. The scattering curves have been shifted vertically for visual clarity.

equatorial radius indicates system forming disk like micelles as temperature increases. Such growth in radius usually comes along with strong intermicellar attractive interaction[45], which is embodied by the decrease of stickiness τ. τ decreases from 0.2 at 40°C to 0.1 at 50°C, indicating stronger attraction at higher temperature. At T > 50°C, the system is approaches a multiphase transition temperature (T=58°C).[1] Equatorial radius jumps from 14.5 nm at 50°C to 34.7 nm at 60°C. This massive increase in length indicates micelle aggregation. At the same time, τ increases from 0.098 at 50°C to 0.24 at 60°C, representing hard sphere repulsion at high temperatures. All of this agrees with previous studies[46]. Above 60°C, the scattering intensity shows distinct difference from other curves. The curve also develops a peak at q ~ 0.221 nm^{-1}(Fig. 5.2B red arrow) and can no longer be described by a single form factor model, indicating the isotropic micelle phase is replaced by the multiphase, which contains polymer rich and polymer poor regions, as reported elsewhere.[1] All of our results for pure Pluronic L62 polymer solutions agree with previous studies.[1,44]

5.4 L62/AOT 25wt%

Charged micelles have been achieved by adding AOT into the L62 micelles at different ratios (L62: AOT = 75:25, 50:50, 25:75) at fixed (5wt%) solute concentration in deuterated water. The scattering intensity of $L62_{0.25}AOT_{0.75}$ solution is shown in Fig. 5.3. At 15°C, the q positions of observed scattering peaks indicate the lamellar structure(L_α). Compared with pure AOT solution (5wt%) at 10°C and 20°C (Fig. 5.1), the shape of peaks indicates that lamellar layers are better aligned, even though the concentration of AOT molecules is lower than that in the pure AOT solution. Additionally, in this trial, the

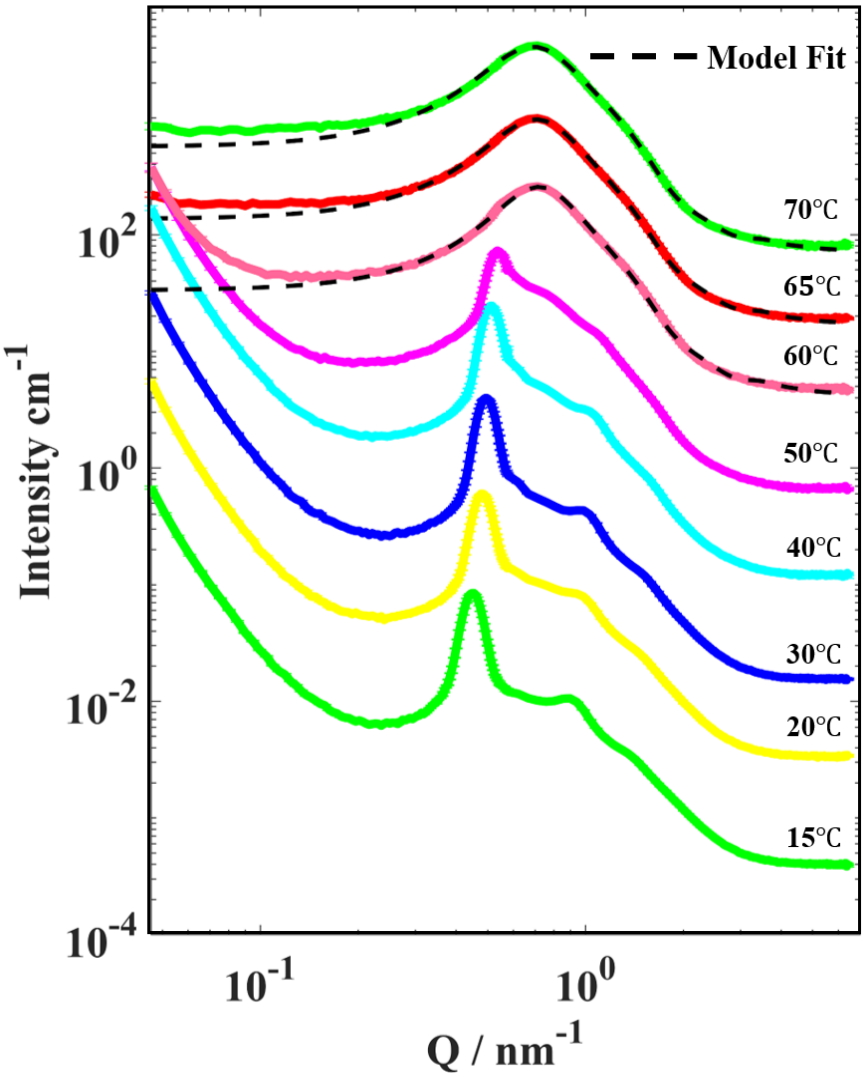

Fig. 5.3 Scattering intensities of 25wt% **(**L62/AOT**)** solution at 10–70°C. The scattering curves have been shifted vertically for visual clarity

lamellar structure eventually collapses around 55°C and transitions to an isotropic phase at high temperatures. In previous study[12], the lamellar(L_α)-Isotropic to micelle(L_1) phase transition temperature depends on the AOT concentration, $T_c \propto$ Concentration. With the concentration(~3.75wt%) in this trail, the pure AOT would go under isotropic phase transition at T ≈ 70°C. As in our case, lamellar structure disappears at 60°C data curve. The L62 micelles seem to undermine the AOT lamellar structure when the temperature increases. We suspect that the solvent quality is poor at high temperatures, so the PPO cores and PEO shells of L62 micelles provide a more energetically favorable location to dissolve the AOT tail groups and head groups, respectively. As shown in Fig.5.3, scattering intensities exhibit reduced features of the lamellar structure at T = 20°C and increased scattering characteristics of micellar phase at increasingly higher temperatures: the broad shoulder after the first peak resembles the features in both 60°C and 70°C data curve and at lower q range. It seems that the addition of L62 copolymer sabotages the persistence of the AOT lamellar structures at high temperature, resulting in an earlier transition of AOT lamellar phase to an isotropic phase and L62-rich micelle phase. The shrinking of spacing, d, as function of temperature agrees with the 5wt% pure AOT trial and a previous study on AOT structure.[47] Scattering intensities above 55°C are fitted with ellipsoid form factor combined with MPB-RMSA structure factor.

5.5 L62/AOT 50wt%

When we increase the fraction of L62 increases to 50wt%, the micellar phase becomes more dominant. At 10°C, L62 copolymers begin process of micelle self-assembly. In Fig.

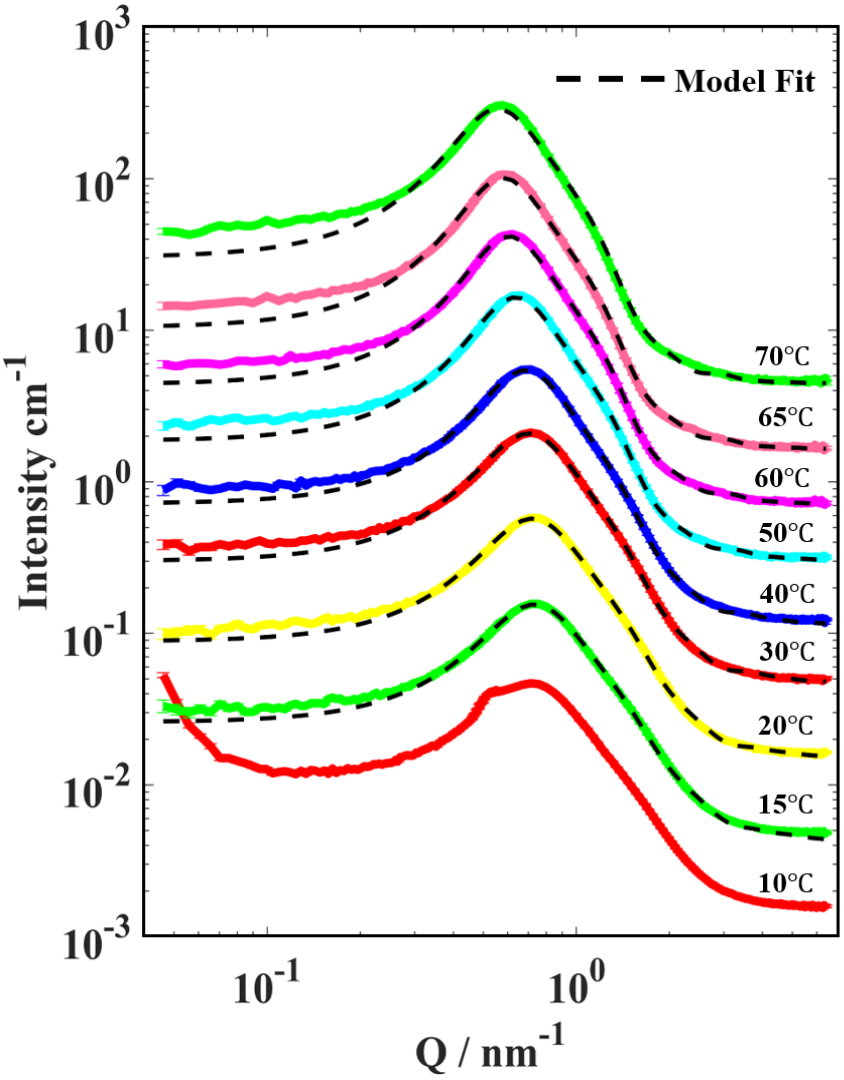

Fig. 5.4 Scattering intensities of 50wt% **(**L62/AOT**)** solution at 10– 70°C. The scattering curves have been shifted vertically for visual clarity

5.4, at 10°C, the intensity curve cannot be described by either the Polymer excluded Volume model or Ellipsoid form factor. The intensity curve also shows large curvature at low q $Å^{-1}$ and the peak around q ≈ 0.03 $Å^{-1}$, meaning that polymer chains have self-assembled and developed an inter-micellar structure, even while AOT lamellar structure and formless polymer chains still exist in the solution. Polymer chains self-assemble into micelles as the temperature goes over 20℃ as expected. In this trial, the isotropic micelle phase dominates. Unlike (L62/AOT)25wt% trail, there is no lamellar structure observed at temperatures above 10℃. As temperature increases, the peak position, which measures the inter-micellar distance, shifts to the lower q, indicating the expansion of inter-micellar distance. We suspect that the increased charge number with temperature leads to the stronger repulsive electrostatic potential between micelles. This results inter-micelle distance increasing with temperature.[45]

Based on the fitting parameters, the micelles' equatorial radius increases from 2.5 nm to 3.2 nm and polar radius increases from 1 nm to 1.7 nm. Charge inside of L62 micelles is measured by applying the MPB-RMSA structure factor and the charge is described by number of extra electrons. As temperature increases from 15°C to 60°C, charges contained in each L62 micelle increases from 12e to 17.2e. The increased charge number indicates that more AOT monomers are involved as building blocks in the formation of L62-rich mixed micelle as the size increases. The charge amount decreases to 16e, as temperature goes over 60°C. A possible explanation is that some of the L62-rich micelles phase transition into multiple phases and cause de-association of AOT monomers in the mixed micelles.

5.6 L62/AOT 75wt%

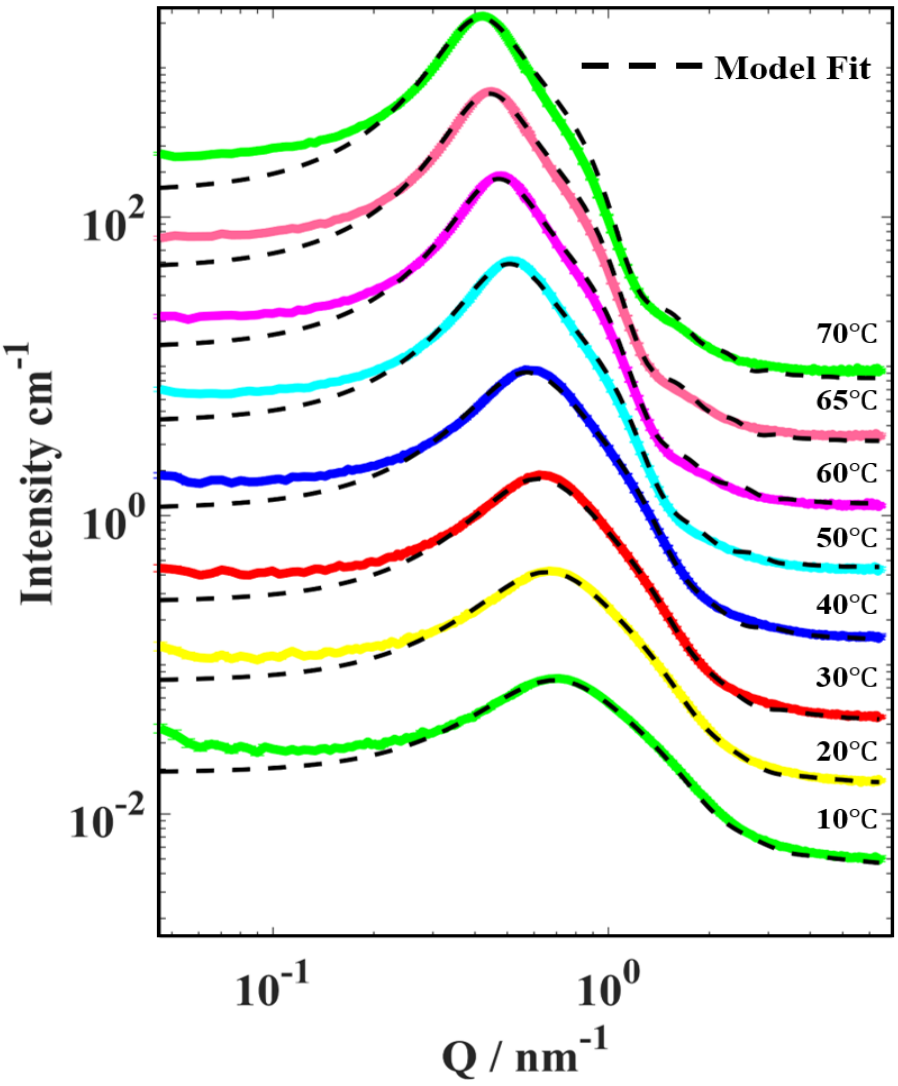

Fig.5.5 Scattering intensities of 25wt% **(**L62/AOT**)** solution at 10– 70°C. The scattering curves have been shifted vertically for visual clarity

In L62/AOT mixture with 75% of L62, formation of micelles occurs at a lower temperature (10 °C) than any other mixture of $L62_xAOT_{1-x}$ studied. This is observed without any signs of an AOT lamellar phase (Fig. 5.5). Mixed micelles exhibit similar

behaviors compared to ones in 50wt.%, and the schematics of mixed micelle is shown in Fig. 5.6. The equatorial radius of the micelles increases from 2.5 nm to 4.0 nm and the polar radius increases from 1.1 nm to 2.6 nm as temperature rises from 10°C to 70°C. In both 50wt% and 75wt.% trails, the EO segments are relatively shrunk at lower tempters and become more extended with increasing temperatures due to better solvent quality. Further, with increasing temperatures, more L62 chains self-assemble into micelles, causing the growth in size and higher ability of containing AOT surfactants, which leads to larger inter-micelle repulsion. The charge monotonically increases from 8.9e to 22.4e in the range of 10°C to 60°C and drops to 21.5e as temperature goes to 70°C, for the reasons explained in the section on (L62:AOT)50wt% trials.

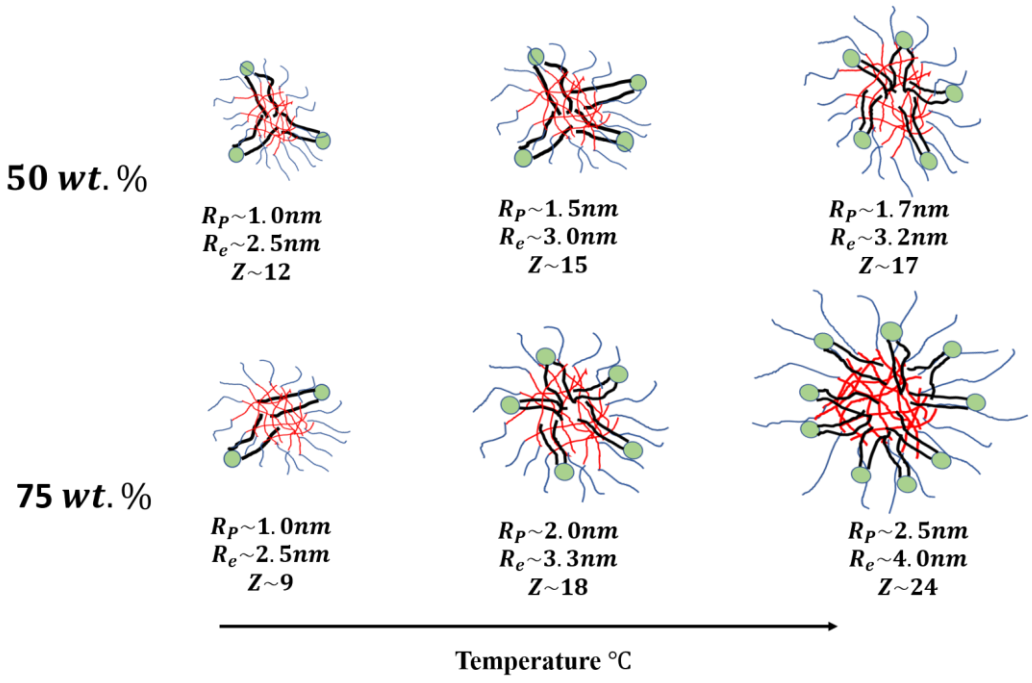

Fig. 5.6 Schematics of L62/AOT mixed micelle structure at L62 relative concentration of $50wt.\%$ and $75wt.\%$. In this schematic, the number of AOT surfactant shown in a micelle does not represent the actual effective charge number but only the charge level of a micelle over temperatures.

5.7 Discussion

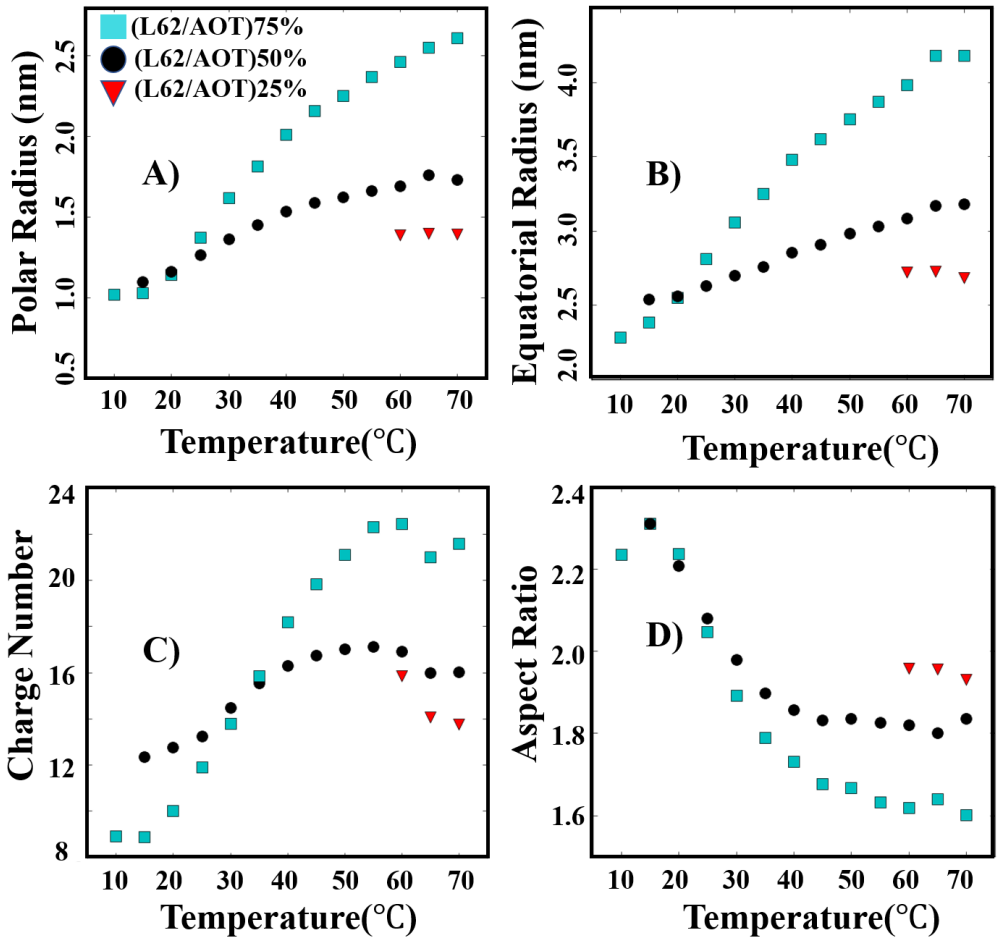

Fig. 5.7 (A-B) Equatorial radius and polar radius of micelles are plotted against temperatures for 25*wt*%, 50*wt*% and 75*wt*% (L62: AOT) sets. (C) Charge number of micelles is plotted vs temperature at 25*wt*%, 50*wt*% and 75*wt*% (L62: AOT). (D) The aspect ratio(ε) is plotted over temperature.

The micellar phase fitting results are summarized in Fig. 5.7 for $L62_xAOT_{1-x}$ (x=0.25, 0.5, 0.75). Overall, an ellipsoid model with charge interaction provides a good fit to most of the scattering data at micellar phase. However, as shown Fig. 5.3 – 5.5, the model consistently underestimates the intensity for lower values of q. We suspect that there are larger AOT aggregations that coexist with the mixed micelle phase. These could provide

extra scattering intensity at low q range. Furthermore, we also observe in the Fig. 5.5 that our fitting model gradually slightly over-predicts the scattering intensity for temperatures above 60℃. This is reasonable because for the (L62/AOT) 75wt.% solution, the phase behavior of L62 is less influenced by the involvement of AOT. As the result, micelle phase partially transitions into a multi-phase, which causes smaller scattering intensity compared to the pure micelle phase. We deduce from the scattering that the overall size of the micelles increases with temperature. This can be explained by large hydrophilic forces that extend the PEO chain in all directions at higher temperatures. The overall size of the mixed micelles increases with higher L62 fractions in the solution, as expected, while the size of the mixed micelles remains much smaller than the size of the pure L62 micelles. One possible reason for this difference is that the addition AOT increases electrostatic repulsion between micelles. This prevents micelles from aggregating and decreases the micelle aggregation number. The aspect ratio decreases monotonically with temperature. Fig. 5.7(D) Aspect ratio, $\varepsilon\ (= R_{\parallel}/R_{\perp})$: $\varepsilon\ <\ 1$ for a prolate spheroid, $\varepsilon = 1$ for a sphere, and $\varepsilon > 1$ for an oblate spheroid. The initial aspect ratio (ε) is around 2.3 for the trial (wt.50%, wt.75%) at 10℃ and as temperature increases, aspect ratio of wt.50% drops to 1.8 and remains constant. On the other hand, the aspect ratio of wt.75% drops to 1.6 and remains constant afterwards. This change in aspect ratio indicates that (1) micelles retain an oblate shape, which becomes less oblate and more spherical with increasing temperature, and (2) with micelles with more L62 polymer chains, are more spherical. The above behavior is in direct contrast to that of pure L62 micelle solutions. In a pure L62 solution, a micelle's equatorial radius increases faster than the polar radius at high temperature, because of the growth of disk like ellipsoid micelles. This results in a high

aspect ratio at high temperature[45]. Charge concentration varies both with temperature and concentrations of AOT. (Fig. 5.7C) For all three trials, the charge contained in the micelles continues to increase as temperature increases until the temperature approaches to 60°C to 65°C and then starts to decrease at even higher temperatures.

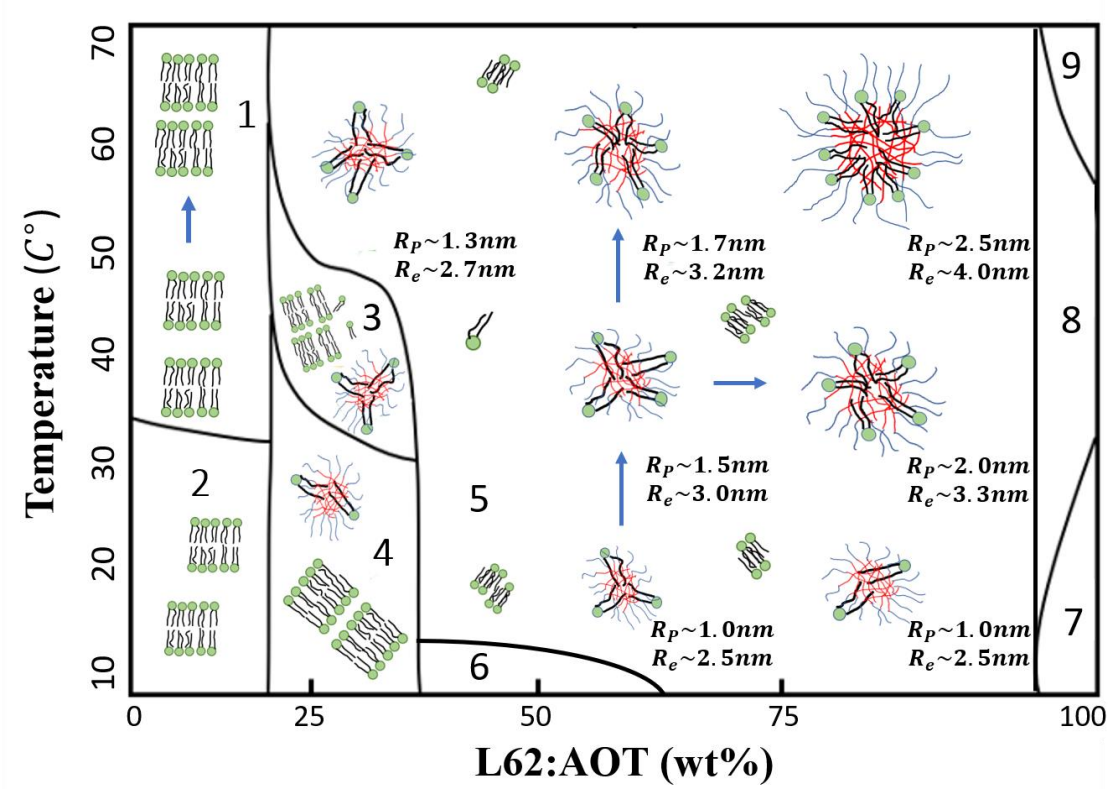

Fig. 5.8 The schematic phase diagram of 5*wt*% (*L*62+*AOT*/D_2O) solution at temperature range of 10°*C* to 70°*C*. (1-2) Lamellar phase(L_α), (3) Lamellar and micelle phase($L_1 \sim L_\alpha$), (4) Lamellar and micelle phase($L_1 < L_\alpha$) (5) Isotropic micelle phase(L_1), (6) Lamellar and micelle phase($L_1 > L_\alpha$), (7) Gaussian chain, (8) Pure L62 micelle phase, (9) Multi-phase region. The number of AOT groups shown in a micelle does not represent the actual effective charge number but the charged level of each micelle.

The result phase behaviors of the SANS on 5wt.% (*AOT* + *L*62) solutions are summarized in the following schematic phase diagram (Fig. 5.8). The phase diagram is composed of 9 regions from 10°C to 70°C at 0, 25,50, 75, 100wt.% (L62: AOT). The temperature and

AOT concentration dependence of L62 micelle sizes and anisotropy has been presented. The schematic phase diagram suggests that addition of AOT helps in the formation of L62 micelles, as observed from $L62_{0.75}AOT_{0.25}$ and $L62_{0.5}AOT_{0.5}$. These temperatures are all below the critical micelle temperature (CMT) of pure L62 copolymer solution (T∼35°C). We suspect that AOT head groups prefer to interact with EO segments of L62, as we mentioned before. There is also a bonded water layer around AOT head group because water molecules of the hydrated sodium ions tend to hydrogen bond to the negatively charged AOT polar head groups.[48] Therefore, it is reasonable to assume that the AOT head groups would interact with PEO hydrophilic segments through bonded the water layer, with PEO acting as a co-surfactant. Such interaction between AOT head groups and PEO segments is synergistic.[49,50] As a result, the critical micelle temperature(CMT) is lower for L62/AOT mixtures than for pure L62 copolymer. Previous studies of L62 copolymer indicates that the isotropic micelle phase is mostly absorbed at temperature above 55°C Fig. 5.8(8). However, in our system, the isotropic micelle phase in L62, AOT mixture remains unabsorbed, even at 70°C.

CHAPTER 6. Conclusions

The thermodynamic phase behaviour of Pluronic L62 (PEO_6)-PPO_{34}-(PEO_6) triblock copolymer has been investigated with various concentration of Aerosol-OT surfactant from 10°C to 70°C through Small Angle Neutron Scattering (SANS). The addition of AOT alters the phase behaviour of L62 solution dramatically. We capture this alteration mainly through the Ellipsoid form factor and MPB-RMSA structure factors. The presence of AOT surfactant creates a synergistic relationship with the L62 micelles, which results in lower critical micelle temperature (CMT) and higher micelle stability compared to non-AOT L62 copolymer solution at high temperatures. As temperature increases, L62 mixed micelles become larger and less anisotropic, directly opposite to the behaviour of pure L62 micelles. The size of the mixed micelles is also much smaller than the pure micelles. We conclude that AOT restrains the L62 polymers from forming rod like micelles at high temperatures due to high intermicellar repulsion. For w/L62(25%), w/L62(50%) and w/L62(75%) mixture solutions, the average charge contained in micelles first increases with temperature and then decreases above 60°C to 65°C. We notice that the charge of the L62 micelles increase with the concentration of AOT in the solution. To explain why two hydrophobic components mix with each other, we propose that the hydrophilic head groups of AOT prefer to interact with the EO segments or with themselves at higher temperatures because of the poor solvent quality of the water. This results in the hydrophilic polymer chains interacting with each other instead of with the solvent molecules. The AOT monomer tail groups also prefer to interact with the PO segments, due to high hydrophobic force. This combination leads to energetically favourable polymer mixing, especially at high temperature, where the stability moves away from the AOT lamellar/L62 micelle phase.

Further, in 50wt% and 75wt% data sets, AOT LLC disappears after 15C and the mixed micelle structure persists from ~15C up to 70C, which is much higher than the multi-phase transition temperature of pure L62. The temperature at which mixed micelles start to form is also much lower than the CMT of pure L62 micelles. Based on our understanding of AOT/L62 system, the mixing behavior of this hydrophobic ionic surfactant and neutral hydrophobic polymer is generally different from hydrophilic SDS mixing with neutral hydrophilic polymer.

REFERENCES

1 P. Alexandridis, D. Zhou and A. Khan, Lyotropic Liquid Crystallinity in Amphiphilic Block Copolymers: Temperature Effects on Phase Behavior and Structure for Poly(ethylene oxide)- *b* -poly(propylene oxide)- *b* -poly(ethylene oxide) Copolymers of Different Composition, *Langmuir*, 1996, **12**, 2690–2700.

2 A. Patel, M. Patel, X. Yang and A. Mitra, Recent Advances in Protein and Peptide Drug Delivery: A Special Emphasis on Polymeric Nanoparticles, *Protein Pept. Lett.*, 2014, **21**, 1102–1120.

3 D. A. Chiappetta and A. Sosnik, Poly(ethylene oxide)-poly(propylene oxide) block copolymer micelles as drug delivery agents: Improved hydrosolubility, stability and bioavailability of drugs, *Eur. J. Pharm. Biopharm.*, 2007, **66**, 303–317.

4 Y. Kadam, U. Yerramilli, A. Bahadur and P. Bahadur, Micelles from PEO-PPO-PEO block copolymers as nanocontainers for solubilization of a poorly water soluble drug hydrochlorothiazide, *Colloids Surfaces B Biointerfaces*, 2011, **83**, 49–57.

5 L. Guo, R. H. Colby, M. Y. Lin and G. P. Dado, Micellar structure changes in aqueous mixtures of nonionic surfactants, *J. Rheol. (N. Y. N. Y).*, 2002, **45**, 1223–1243.

6 Y. Li, R. Xu, D. M. Bloor, J. F. Holzwarth and E. Wyn-Jones, Binding of sodium dodecyl sulfate to the ABA block copolymer pluronic F127 (EO97PO69EO97): An electromotive force, microcalorimetry, and light scattering investigation, *Langmuir*, 2000, **16**, 10515–10520.

7 P. Alexandridis, J. F. Holzwarth and T. A. Hatton, Micellization of Poly(ethylene oxide)-Poly(propylene oxide)-Poly(ethylene oxide) Triblock Copolymers in Aqueous Solutions: Thermodynamics of Copolymer Association, *Macromolecules*, 1994, **27**, 2414–2425.

8 M. Almgren, J. Van Stam, C. Lindblad, P. Li, P. Stilbs and P. Bahadur, Aggregation of poly(ethylene oxide)-poly(propylene oxide)-poly(ethylene oxide) triblock copolymers in the presence of sodium dodecyl sulfate in aqueous solution, *J. Phys. Chem.*, 1991, **95**, 5677–5684.

9 I. E. Pacios, C. S. Renamayor, A. Horta, B. Lindman and K. Thuresson, Equilibrium between poly(N,N-dimethylacrylamide) and the lamellar phase of aerosol OT/water, *J. Phys. Chem. B*, 2002, **106**, 5035–5041.

10 E. Signal and P. Conference, SINGLE MICROPHONE WIND NOISE REDUCTION USING TECHNIQUES OF ARTIFICIAL BANDWIDTH EXTENSION Institute of Communication Systems and Data Processing ( ) RWTH Aachen University , Germany Intel Mobile Communications , Sophia-Antipolis , France, *2012 Proc. 20th Eur. Signal Process. Conf.*, 2012, 2328–2332.

11 P. Alexandridis, J. F. Holzwarth and T. A. Hatton, Micellization of Poly(ethylene oxide)-Poly(propylene oxide)-Poly(ethylene oxide) Triblock Copolymers in Aqueous Solutions: Thermodynamics of Copolymer Association, *Macromolecules*, 1994, **27**, 2414–2425.

12 Z. X. Li, A. Weller, R. K. Thomas and A. R. Rennie, Adsorption of the Lamellar Phase of Aerosol-OT at the Solid / Liquid and Air / Liquid Interfaces, *J Phys Chem B*, 1999, **103**, 10800–10806.

13 K. Zhang and P. Linse, Solubilization of polymer in the lyotropic lamellar phase: The AOT/PEO/water system, *J. Phys. Chem.*, 1995, **99**, 9130–9135.

14 M. F. Ficheux, A. M. Bellocq and F. Nallet, Effect of two water-soluble polymers on the stability of the AOT-H2O- lamellar phase, *Colloids Surfaces A*

Physicochem. Eng. Asp., 1997, **123**–**124**, 253–263.
15 P.Lindner and Th.Zemb, in *Neutrons, X-rays and Light: Scattering Methods Applied to Soft Condensed Matter*, 2002, p. 5.
16 M. Kotlarchyk and S. H. Chen, Analysis of small angle neutron scattering spectra from polydisperse interacting colloids, *J. Chem. Phys.*, 1983, **79**, 2461–2469.
17 J. S. Pedersen, Form and Structure Factors: Modeling and Interactions, *J. R. Soc. Interface*, 2010, **6**, 235–239.
18 O. Gang, Small Angle X-Ray Scattering (SAXS) from Bulks and Surfaces, *Small Angle X-Ray Scatt. from Bulks Surfaces*.
19 L A Feigin and D I Svergun, *Structure Analysis by Small-Angle X-Ray and Neutron Scattering*, 1987.
20 A. In, Encyclopedia of Contemporary Literary Theory, *Encycl. Contemp. Lit. Theory*, 2018, **70**, 171–210.
21 B. Hammouda, Chapter 28 - FORM FACTORS FOR POLYMER SYSTEMS, *PROBING NANOSCALE Struct. – Sans Toolbox*, 2010, 1–13.
22 S. P. The, T. H. E. Guinier and P. The, Porod region, 1–17.
23 D. A. McQuarrie, in *Statistical Mechanics*, 1973, pp. 36–50.
24 D. A. McQuarrie, in *Statistical Mechanics*, 1973, pp. 52–55.
25 D. A. McQuarrie, in *Statistical Mechanics*, 1973, pp. 223–253.
26 D. A. McQuarrie, in *Statistical Mechanics*, 1973, pp. 254–269.
27 D. A. McQuarrie, in *Statistical Mechanics*, 1973, pp. 298–299.
28 J. B. Hayter and J. Penfold, An analytic structure factor for macroion solutions, *Mol. Phys.*, 1981, **42**, 109–118.
29 M. Heinen, P. Holmqvist, A. J. Banchio and G. Ngele, Pair structure of the hard-sphere Yukawa fluid: An improved analytic method versus simulations, Rogers-Young scheme, and experiment, *J. Chem. Phys.*, , DOI:10.1063/1.3524309.
30 J. S. Høye and L. Blum, Solution of the Yukawa closure of the Ornstein-Zernike equation, *J. Stat. Phys.*, 1977, **16**, 399–413.
31 J. P. Hansen and J. B. Hayter, A rescaled MSA structure factor for dilute charged colloidal dispersions, *Mol. Phys.*, 1982, **46**, 651–656.
32 JAN K.G. DHOUT, in *An Introduction to Dynamics of Colloids*, 1996, p. 109.
33 P.Lindner and Th.Zemb, in *Neutrons, X-rays and Light: Scattering Methods Applied to Soft Condensed Matter*, 2002, p. 3.
34 JAN K.G. DHOUT, in *An Introduction to Dynamics of Colloids*, 1996, p. 113.
35 P.Lindner and Th.Zemb, in *Neutrons, X-rays and Light: Scattering Methods Applied to Soft Condensed Matter*, 2002, p. 20.
36 P.Lindner and Th.Zemb, in *Neutrons, X-rays and Light: Scattering Methods Applied to Soft Condensed Matter*, 2002, p. 16.
37 P.Lindner and Th.Zemb, in *Neutrons, X-rays and Light: Scattering Methods Applied to Soft Condensed Matter*, 2002, p. 14.
38 P.Lindner and Th.Zemb, in *Neutrons, X-rays and Light: Scattering Methods Applied to Soft Condensed Matter*, 2002, p. 29.
39 P.Lindner and Th.Zemb, in *Neutrons, X-rays and Light: Scattering Methods Applied to Soft Condensed Matter*, 2002, p. 39.
40 P.Lindner and Th.Zemb, in *Neutrons, X-rays and Light: Scattering Methods Applied to Soft Condensed Matter2*, 2002, pp. 30–33.
41 J. S. PEDERSEN, Resolution effects and analysis of small-angle neutron scattering data, *Le J. Phys. IV*, 1993, **03**, C8-491-C8-498.
42 S. R. Kline, Reduction and analysis of SANS and USANS data using IGOR Pro, *J. Appl. Crystallogr.*, 2006, **39**, 895–900.
43 Z. X. Li, a. Weller, R. K. Thomas, a. R. Rennie, J. R. P. Webster, J. Penfold, R.

K. Heenan and R. Cubitt, Adsorption of the Lamellar Phase of Aerosol-OT at the Solid/Liquid and Air/Liquid Interfaces, *J. Phys. Chem. B*, 1999, **103**, 10800–10806.

44 Y. Han, Z. Zhang, G. S. Smith and C. Do, Effect of nucleoside analogue antimetabolites on the structure of PEO-PPO-PEO micelles investigated by SANS, *Phys. Chem. Chem. Phys.*, 2017, **19**, 15686–15692.

45 R. Ganguly, N. Choudhury, V. K. Aswal and P. A. Hassan, Pluronic L64 micelles near cloud point: Investigating the role of micellar growth and interaction in critical concentration fluctuation and percolation, *J. Phys. Chem. B*, 2009, **113**, 668–675.

46 K. Mortensen and J. S. Pedersen, Structural Study on the Micelle Formation of Poly(ethylene oxide)–Poly(propylene oxide)–Poly(ethylene oxide) Triblock Copolymer in Aqueous Solution, *Macromolecules*, 1993, **26**, 805–812.

47 Z. X. Li, A. Weller, R. K. Thomas and A. R. Rennie, Adsorption of the Lamellar Phase of Aerosol-OT at the Solid / Liquid and Air / Liquid Interfaces, *J Phys Chem B*, 1999, **103**, 10800–10806.

48 T. K. Jain, M. Varshney and A. Maitra, Structural studies of aerosol OT reverse micellar aggregates by FT-IR spectroscopy, *J. Phys. Chem.*, 1989, **93**, 7409–7416.

49 T. Thurn, S. Couderc, J. Sidhu, D. M. Bloor, J. Penfold, J. F. Holzwarth and E. Wyn-Jones, Study of mixed micelles and interaction parameters for ABA triblock copolymers of the type EOm-POn-EOmand ionic surfactants: Equilibrium and structure, *Langmuir*, 2002, **18**, 9267–9275.

50 H. Kunieda, K. Ozawa, K. Aramaki, A. Nakano and C. Solans, Formation of Microemulsions in Mixed Ionic−Nonionic Surfactant Systems, *Langmuir*, 2002, **14**, 260–263.